Formation Flying Performance Measures for Earth-Pointing Missions

Steven P. Hughes

Thesis submitted to the Faculty of the

Virginia Polytechnic Institute and State University

in partial fulfillment of the requirements for the degree of

Master of Science

in

Aerospace Engineering

Dr. Christopher Hall - chair

Dr. Frederick Lutze

Dr. Mary Kasarda

December 1999

Blacksburg, Virginia

Formation Flying Performance Measures for Earth-Pointing Missions

Steven P. Hughes

(ABSTRACT)

Clusters of low-performance spacecraft flying in formation may provide enhanced performance over single high-performance spacecraft. This is especially true for remote sensing missions where interferometry or stereographic imaging may provide higher resolution data. The configurations of such formations vary during an orbit due to orbital dynamics, and over longer time scales due to perturbations. Selection of a configuration should be based on overall performance of the formation. In this thesis, performance measures are developed and evaluated based on integration over one orbit. The measures involve the angular separation of spacecraft, the distance between spacecraft, and an area-based measure of the separation of the spacecraft. Numerical techniques are employed to evaluate the performance measures to determine optimal scenarios for two formations. Simplifying assumptions are made to allow a closed-form analytic solution and the results are compared to those obtained numerically. Finally, the sensitivity of the measures to linearized propagation techniques is investigated.

Acknowledgments

As in any work with the magnitude of a thesis, the author is indebted to many people for the content and shape that the finished product assumes. In this case the debt of gratitude is no exception, and in fact extends beyond the ordinary. I wish to thank first and foremost my graduate advisor Dr. Christopher Hall. His infectious enthusiasm and untiring patience and support were an essential component in the completion of this research. He maintained an open door policy throughout the course of this work, and was willing to drop whatever he was working on when I needed help with something or had an idea to discuss. I would also like to thank Mr. David Folta, Mr. David Weidow, and Mr. Tom Stengle for both financial and moral support. Thanks is also due to Dr. Fred Lutze and Dr. Mary Kasarda for taking the time to be on my graduate committee and to review the final draft. And last but certainly not least I would like to thank my family and friends for their moral support and encouragement.

Contents

List of Figures

List of Tables

Chapter 1

Introduction

The study of formation flying involves many fields of engineering and science including orbital dynamics, attitude dynamics, remote sensing, communications, and systems engineering. In this chapter we investigate the advantages and disadvantages of using a distributed array of spacecraft in light of the science and engineering challenges. We also review the literature to determine areas that need more attention. In the final section of this chapter we present the framework for our discussion of performance measures for formation flying missions.

1.1 The Formation Flying Concept

The formation flying concept has recently become popular due to its potential in coordinated measurements for remote sensing missions and flexible long-term mission capabilities. Clusters of low-performance spacecraft flying in formation may provide enhanced performance

over single high-performance spacecraft. This is especially true for remote sensing missions where interferometry or stereographic imaging may provide higher resolution data.

The benefits of formation flying spacecraft are substantial in many areas of space mission architecture. A multiple spacecraft platform allows increased flexibility to include new technology into preexisting missions. Hence as higher resolution instruments are developed or new areas of scientific interest are realized, existing missions can be modified to incorporate them. The use of several small satellites with a suite of instruments on each to replace a single large platform increases the likelihood of mission success in the event of a malfunction.

Perhaps the single most significant driver for formation flying spacecraft is the ability to perform coordinated yet distributed measurements. The difference in perspective achieved by spacecraft within a formation can provide higher resolution data through the use of techniques in stereographic viewing, synthetic aperture radar, and radio-interferometry.[1,2] Significant improvements in atmospheric and gravity modeling are also possible.[1]

Although the benefits are numerous, formation flying missions have many difficulties that single platform missions do not. For large formations multiple launches may be required which leads to difficulty in formation establishment and initialization. To ensure a cohesive formation, a common semimajor axis must be maintained for all spacecraft in the formation. Inter-satellite communications are necessary to ensure that the desired relative navigation and pointing are achieved once the formation is operational. There is an obvious increase in the navigational and attitude control requirements to ensure proper relative motion. However, recent advances in spacecraft autonomy in both navigation and attitude

control permit the implementation of multiple spacecraft missions that were not feasible even in the early nineties.

Navigational complications arise due to orbital mechanics and over long time scales due to perturbations. A static formation, in which there is no relative motion between spacecraft, is only possible for satellites in circular, coplanar orbits. For non-coplanar, non-circular orbits there is relative motion in both the along-track and cross-track directions. Other navigational complications arise when ground-track control is required or when sun-synchronous orbit planes or frozen orbits are desired.

Perturbations due to atmospheric drag and non-spherical gravity effects also require station-keeping strategies. Spacecraft with different ballistic coefficients will have different orbit decay rates and can be expected to have a secular drift with respect to each other over long time scales. The difference in drag can be used in a formation control strategy and has been studied by Folta.[3] Because spacecraft in formation may be separated by distances on the order of kilometers to hundreds of kilometers, they may be influenced by the Earth's aspherical gravity field differently and drift relative to one another.

We now review the literature on the formation flying concept and its applications. This includes a variety of subject areas including orbit dynamics and control issues, relative pointing dynamics, GPS navigation possibilities, and communications requirements.

1.2 Previous Work

A preliminary feasibility study of formation flying technologies was performed by Folta *et al.*[4] In this work the pointing and navigational requirements were investigated to maintain an 80% field of view overlap between two spacecraft in polar orbits. Assuming the attitude errors to have a guassian distribution and modeling expected ground track drift, the authors determined that technology at the time of the study was not capable of meeting such a requirement. Further investigations were performed by Folta *et al.*[3] to understand how to relate observations from two spacecraft, to determine the effects of perturbations, and to confirm previous results. Two formations were considered: a master-slave scenario where one spacecraft moves relative to a reference spacecraft, and a constant-time separation scenario. For each formation two attitude models were assumed: a perfect local horizontal, local vertical orientation, and an attitude based on the maximum allowable tolerance offset for requirements for attitude determination. Again the requirement that the field-of-view overlap must meet or exceed 80% was applied. The authors determined that even neglecting random attitude errors, only a close formation, separated by one hundred meters or less in the orbit velocity direction, could meet mission requirements using technology at the time of study.

Orbital station-keeping and navigational algorithms have received significant attention in the literature. DeCou[2] developed a three-satellite station-keeping strategy describing paths to perform very long baseline optical interferometry. The paths lie in a plane perpendicular to the direction of the astronomical object of interest to maximize the use of gravity gradient

torques and minimize thrust. DeCou concluded that the thrusting required is low enough to allow missions of up to ten years using ion thrusters without refueling.

The formation flying concept was revisited by Folta *et al.*[5] in 1996 and the feasibility of formation flying for particular missions in light of new advances in technology and autonomy was investigated. Specifically, the application of formation flying concepts to the Mission to Planet Earth (MTPE) and New Millennium (NM) programs were studied. Characteristic relative motion of a formation flyer with respect to a reference orbit was presented using the Clohessy-Wiltshire equations as a mathematical model. The dynamics of an uncontrolled formation with and without atmospheric drag was studied. Finally a formation control strategy for the Earth Observing System-AM1 (EOS-AM1) and Landsat-7 was investigated using a dynamic ballistic coefficient strategy.

Formation flying involves both "formation sensing" and "formation control" as described by Gramling *et al.*[6] Formation sensing is the process of determining the relative position of satellites in formation. The relative position information is then used as input to a formation control algorithm. Gramling demonstrated the possibility of using Goddard Space Flight Center's (GSFC) Onboard Navigation System (ONS) for relative navigation of the EO-1/Landsat-7 spacecraft formation. A strategy was presented for using ONS for real time formation sensing. In the hypothesized scenario the target spacecraft estimated the relative position of the chase spacecraft based on Doppler measurements derived from a cross-link communications signal. The position of the target spacecraft was determined independently using GPS. The state information for the chase spacecraft was then used

by the autonomous maneuver control software onboard the target spacecraft to plan the maneuvers for the formation. The intention of the strategy was to reduce mission control ground efforts. Results of the simulated ONS performance for a coplanar and a non-coplanar formation were presented. For both scenarios ONS was demonstrated to be capable of estimating the relative position with enough accuracy for successful formation control.

Hartman *et al.*[7] extended the study of GSFC's ONS performance for spacecraft formation flying. Specifically Hartman investigated orbit determination and prediction accuracies and their impact on the relative separation errors. As in the work by Gramling *et al.*,[6] the model used was the EO-1/Landsat-7 formation. To perform formation control, the relative radial position and velocity of the spacecraft must be known to within 5 m and 2.7 cm/s respectively. Although the requirements are stringent, ONS was found to be capable of meeting them.

The use of GPS for relative navigation of formation flying spacecraft has been studied by Guinn *et al.*[8] and for both relative position and attitude sensing by Adams *et al.*[1] and How *et al.*[9] Adams *et al.*[1] presented results from a GPS-based relative navigation and attitude sensing system developed in the laboratory. A formation was modeled using four air-cushioned vehicles on a granite table top. Absolute versus relative control architectures were investigated as well as the communication requirements for each. In the absolute control architecture, position and velocity commands were sent to each spacecraft from a central controller. The relative controller architecture utilized a "leader" spacecraft which was sent absolute postion/velocity requirements from the controller. The remaining spacecraft at-

tempted to maintain relative positions with respect to the leader. Tests determined that the absolute control method performed better for maneuvers mainly because there was a lag in the follower vehicles' motion for the relative control architecture. However, the authors deemed both methods feasible for formation control.

The extension of autonomous orbit determination and control using GPS to multiple spacecraft flying in formation was investigated by Guinn *et al.*[8] using the EO-1/Landsat-7 mission as a model. Orbit determination accuracies for several types of GPS solutions were presented. For non-military use the GPS satellite system offers position information advertised at accuracies of one hundred meters horizontal and one hundred and forty meters vertical.[8] These measurements are possible in the Selective Availability mode which intentionally degrades the process to produce less accurate solutions than those obtainable by military users. Improvements in the advertised capabilities were made by computing the RMS of the total position differences of the onboard navigation solutions and precision orbit ephemeris. Other improvements were also demonstrated using an extended Kalman filter. Accuracies on the order of 5 m are possible after allowing a settling time of about 4 hours. Because EO-1 and Landsat-7 have different frontal areas and masses they will have different ballistic coefficients and hence will be affected by atmospheric drag differently. The difference in atmospheric drag will primarily affect the along-track separation due to the differential semimajor axis of the two spacecraft. The authors presented an analytical method for determining the expected ΔV required to keep the spacecraft within the acceptable control boundary.

The possibility of formation flying in the vicinity of libration points was studied by Barden *et al.*[10] The authors discussed the types of motion that exist near libration points and the types of transitions between them. Manifold theory was used to investigate the option of formation flying in the vicinity of a libration point. An example was shown using a six-spacecraft formation and the evolution of the orbits was demonstrated.

Guinn[11] studied the effects of various perturbations including aspherical gravity, atmospheric drag, solar radiation pressure, and third body gravity, on the relative motion of space vehicles in formation. High-fidelity force models were used to characterize the relative motion effects due to each perturbation for circular LEO and GEO orbits as well as for circular low and synchronous Mars orbits.

Folta and Quinn[12,13] developed an algorithm for autonomous, closed-loop, three-axis navigation and control for spacecraft in formation using GPS navigation support. The algorithm attempts to zero the difference between the actual state and the desired state determined by state estimation software such as ONS. Given an allowable maneuver window, a possibly non-Keplerian trajectory is calculated based on the initial and final states and the time allowed for the maneuver. The reference trajectory is broken down into a series of control points over regular time intervals that allow the spacecraft to receive position information, fire thrusters, and account for the firing. At each control point the spacecraft's actual position is compared to its desired location on the reference trajectory. A linearized state transition matrix is then used to compute the necessary ΔV required to get the spacecraft to the next control point on the reference trajectory. The algorithm was applied to several

formation configurations using high-fidelity simulation tools.

The use of a distributed architecture for space-based radar was investigated by Wickert *et al.*[14] The authors investigated the feasibility of using a constellation of satellites that provides global multifold coverage to perform the same function as the current airborne warning and control system. A cluster of satellites within the constellation acts as a formation to provide a local distributed array. The analysis used a metric based on the cost to initialize the array and the initial operating capability. The cost function was optimized in terms of orbital altitude, cluster size, satellite power and aperture, area search rate and redundancy. From these variables all other system variables may be derived. The authors determined that to minimize cost, the distribution should be greater than that necessary to provide global coverage. This allows several satellites to view the same region simultaneously. When redundancy is employed the optimum cluster size available to search a given region is between three and five.

Chichka[15] investigated the dynamics of formations that maintain a constant shape when viewed from the surface of the Earth. The motion is described with respect to a reference satellite in a circular orbit denoted the reference orbit. The relative reference frame is centered on the reference satellite with the x, y, and z unit vectors in the radial, velocity, and orbit normal directions, respectively. Using this frame of reference Chichka developed elliptical relative orbits using the Clohessy-Wiltshire equations. The dimensions of the orbits were characterized in terms of the eccentricity, orbit radius, and the inclination. Because the Clohessy-Wiltshire equations are linear approximations, Chichka also developed corrections

due to the first-order approximation.

Formation flying spacecraft is a relatively new concept which still requires significant research in many areas of space mission architecture. In fact, at the time of this study, there are no active missions using formation flying technology. Perhaps the single most significant driver for formation flying is the ability to perform coordinated yet distributed measurements. However, missions that employ a distributed array of spacecraft have complications that single-spacecraft missions do not. A formation configuration must be capable of meeting demanding mission requirements and constraints. Yet there is little treatment in the literature on performance measures for evaluating the effectiveness of formation configurations.

1.3 Overview of the Thesis

Clusters of low-performance spacecraft flying in formation may provide enhanced performance over single high-performance spacecraft. Furthermore, multiple spacecraft missions allow the application of remote sensing techniques not possible for single satellite missions. The configuration of such formations vary during an orbit due to orbital dynamics, and over longer time scales due to perturbations. Selection of a configuration should be based on overall performance of the formation. However, formation performance has not received significant attention in the literature.

The difference in perspective provided by a distributed array of spacecraft allows the application of remote sensing techniques not possible for single satellite missions. The relative

positions of spacecraft in a formation must satisfy required tolerances defined by mission requirements. Therefore, the ability of a formation to perform a desired mission is determined by the relative motion of the spacecraft in formation over the course of an orbit. At a given instant, the configuration of a formation must allow multiple spacecraft to view a target simultaneously. Acceptable separations must also be maintained over the evolution of the orbits.

In this thesis we review the orbital dynamics concepts required to investigate the dynamics of spacecraft flying in a distributed array. We briefly review remote sensing missions concepts to gain appropriate insight needed to develop useful performance measures. We develop several metrics to evaluate the performance of a formation of spacecraft based on orbital dynamics and remote sensing concepts. Instantaneous measures are developed to investigate the state of a formation at a given instant. Orbit performance measures are developed based on the integration of an instantaneous performance metric over one orbit.

The performance measures are applied to two different formations which we call the diamond and the rotating formation. In general the metrics do not permit exact analytic solutions. Numerical integration techniques are applied to obtain solutions for the measures. The effect of changing orbit parameters such as semimajor axis and eccentricity is characterized. We show that a closed-form analytic solution for one of the orbit performance measures when applied to the rotating formation is possible with some simplifying assumptions. The results of the analytic approximation are compared to the exact numerical results. Finally the performance measures are evaluated using the Clohessy-Wiltshire first order relative mo-

tion solution. The sensitivity of the orbit performance measures to errors in propagation is investigated.

Chapter 2

Formation Modeling

To develop and evaluate formation performance measures we first develop a mathematical model for a formation of spacecraft. This includes determining the relevant forces for the orbital equation of motion, and the most useful form of its solution. We also determine which numerical tools allow an efficient evaluation of the measures. To ensure a cohesive formation, we also consider constraints on the orbits as well as some simplifying assumptions.

2.1 Orbit Modeling

Spacecraft are subject to disturbing forces such as atmospheric drag, solar radiation pressure, and third body effects as well as the non-spherical central body force. Evaluation of the orbit performance measures developed in Ch. 3 requires knowledge of the position of all spacecraft in the formation over an orbital period. For a comparative study of candidate orbits the

performance measures must be evaluated for many different initial states, resulting in a large number of orbit integrations. High-fidelity force models are computationally expensive but are not expected to have a significant effect on preliminary formation design. Therefore, to simplify the preliminary analysis, we neglect the disturbing forces and approximate the orbital dynamics with Keplerian motion.

The Keplerian orbital dynamics problem is defined by the differential equation

$$\ddot{\mathbf{r}} = -\mu \frac{\mathbf{r}}{r^3} \tag{2.1}$$

where $\mathbf{r}$ is the position vector of the satellite and r is the magnitude of the position vector. The gravitational parameter, μ, is a physical constant dependent upon the mass of the central body. There are three degrees of freedom and six independent states. We therefore need six independent constants to define the motion uniquely. In this thesis we use the classical orbital elements: the semimajor axis a, the eccentricity e, the inclination i, the argument of periapsis ω, the longitude of ascending node Ω, and the time past periapsis τ. To locate a spacecraft within the orbit we use the true anomaly ν.

For Keplerian motion an orbit lies in a fixed plane in the inertial frame $\mathcal{F}_I$. The origin of the inertial frame is the center of the Earth and the $\hat{\mathbf{i}}$-axis points in the direction of the vernal equinox. The $\hat{\mathbf{j}}$-axis also lies in the equatorial plane and points 90° to the east of the $\hat{\mathbf{i}}$-axis. The $\hat{\mathbf{k}}$-axis points in the direction of the North Pole. The inclination and the longitude of ascending node orient the orbital plane in $\mathcal{F}_I$ as seen in Fig. 2.1. The inclination is defined as the angle between the orbit normal vector, $\hat{\mathbf{n}}$, and the $\hat{\mathbf{k}}$-axis. The range of i

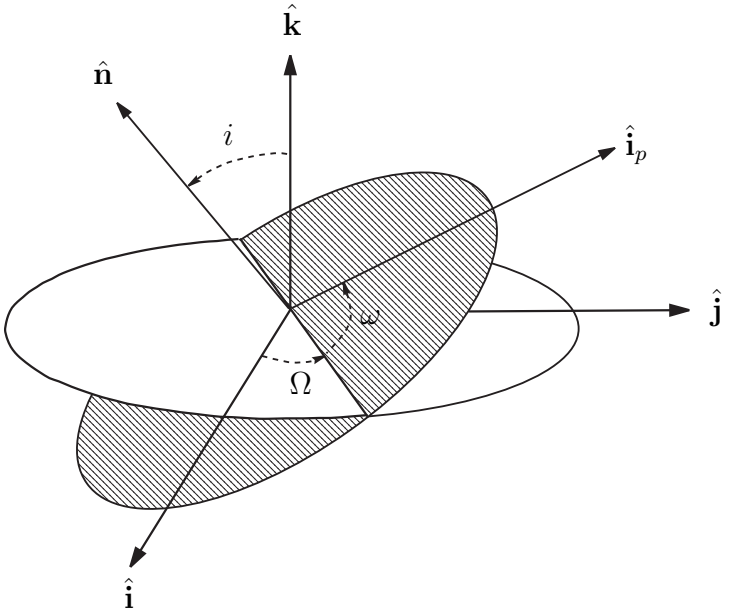

Figure 2.1: The Orbital Elements and Orbit Geometry

is between 0° and 180°. A spacecraft will pass through the equatorial plane twice in one orbit. The ascending node is the point at which a spacecraft crosses the equatorial plane going from the southern to the northern hemisphere. The longitude of ascending node is the angle between the $\hat{\mathbf{i}}$-axis and the ascending node measured positively to the east.

The variables a, e and ω define the shape and position of the orbit within the orbital plane and ν locates the satellite within the orbit. In this thesis we are only concerned with elliptical orbits. A common system for representing elliptical orbit properties is the perifocal system, $\mathcal{F}_p$. The perifocal system is shown Fig. 2.2. The origin of the perifocal system is at the center of the Earth. The $\hat{\mathbf{i}}_p$-axis points in the direction of the periapsis, the point of closest approach for a spacecraft in orbit. The $\hat{\mathbf{j}}_p$-axis lies in the orbital plane and is rotated 90° from the $\hat{\mathbf{i}}_p$-axis in the direction of motion. The $\hat{\mathbf{k}}_p$-axis is normal to the orbital plane.

Elliptical orbits have geometric properties based on a and e. The size of the orbit is

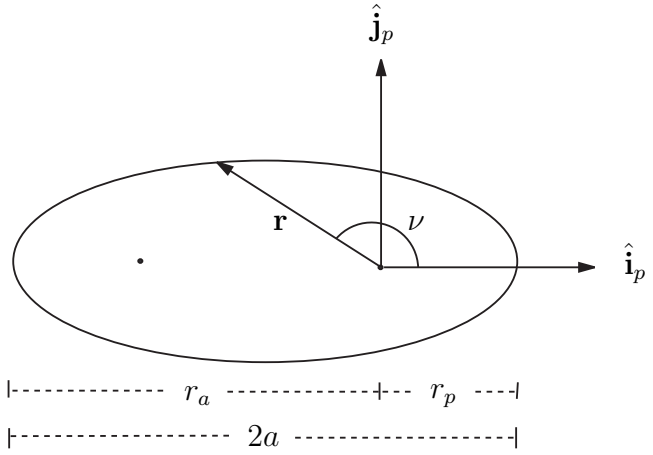

Figure 2.2: Elliptical Orbit Geometry

determined by the semimajor axis. The eccentricity determines the shape of the orbit and the distances r_p and r_a. The distance r_p is called the radius of periapsis and is the point of closest approach. The radius of periapsis is given by

$$r_p = a(1 - e) \tag{2.2}$$

The distance r_a is called the radius of apoapsis and is the point where a spacecraft is farthest from the Earth. The radius of apoapsis can be written

$$r_a = a(1 + e) \tag{2.3}$$

The argument of periapsis, ω, is defined as the angle between the periapsis vector $\hat{\mathbf{i}}_p$ and the ascending node measured positively in the orbital plane. The argument of periapsis locates the periapsis of the orbit and orients the ellipse in the orbital plane. To locate a satellite's position within its orbit we use the true anomaly, the angle between $\hat{\mathbf{i}}_p$ and the

spacecraft position vector, $\mathbf{r}$. For circular orbits $e = 0$. Hence $r_a = r_p$ and ω and ν are undefined. In this case we locate the spacecraft in the orbital plane using the argument of latitude at epoch, u. The argument of latitude at epoch is the angle between the ascending node and $\mathbf{r}$. For circular, equatorial orbits ω, Ω, and ν are undefined and we locate the position of a satellite in the equatorial plane using ℓ, the true longitude at epoch. For a more detailed discussion on the orbital elements see Bate *et. al.*[16]

2.2 Formation Constraints and Considerations

Recall that for a formation composed of n satellites there are $3n$ degrees of freedom and $6n$ states. The large number of state variables makes it difficult to examine the change in a performance measure due to changes in the initial state. We wish to explore the design space of a formation by decreasing the number of state variables used to define a formation uniquely.

To ensure the formation's periodic motion over an orbit we require that all orbits in the formation have the same period. Therefore all of the spacecraft must have the same semimajor axis because the period depends only on μ and a:

$$T = 2\pi\sqrt{\frac{a^3}{\mu}} \tag{2.4}$$

If all the spacecraft in a formation do not have the same period then eventually separation will occur and simultaneous viewing of a target will be impossible. If we hold the semimajor axis constant for all satellites we decrease the number of state variables from $6n$ to $5n$.

A further reduction in order is achieved by referencing all spacecraft to one of the spacecraft in the formation. Because the performance measures developed in Ch. 3 are not dependent on absolute position with respect to the Earth, only on the relative position of spacecraft, there is no loss of generality in doing so. We are simply picking one of a family of solutions that will result in the same weight function value over an orbit. We can justify this by realizing that there is an infinite number of state vectors, such that the relative motion of the spacecraft will be the same, only shifted in position with respect to the Earth. Eliminating the variables used to define the reference orbit we are left with $5(n-1)$ state variables to describe a formation uniquely.

The separation between two spacecraft in formation can be conveniently described by two quantities. The angle between the position vectors of two spacecraft is defined as the angular separation, α. The distance, d, is the spatial separation between two spacecraft. The quantities d and α are related by a simple geometric relation:

$$\sin\left(\frac{\alpha}{2}\right) \approx \frac{d}{2a} \tag{2.5}$$

For circular orbits with the same a this relation is exact. However, we will consider formations with small yet non-zero eccentricities, in which case the relation is approximate. Figure 2.3 shows lines of constant angular separation for a range of d and a relevant to the work in this thesis. For constant a increasing d causes an increase in α. However, for constant d increasing a results in a decrease in α.

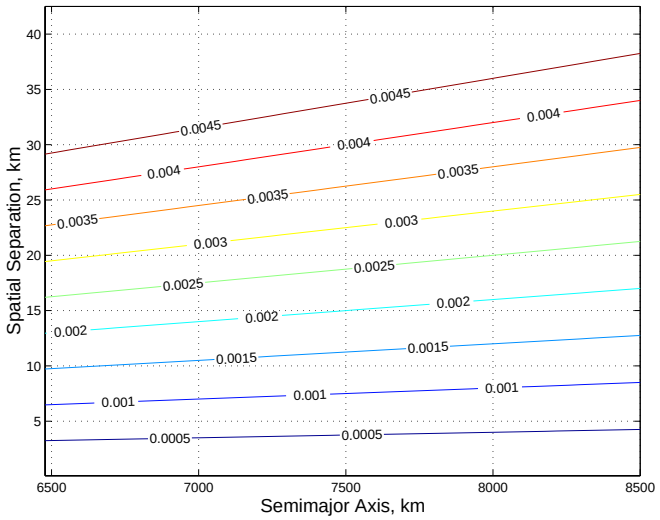

Figure 2.3: Lines of Constant α *vs.* r and a

2.3 Numerical Techniques

A closed-form analytic solution to the orbit performance measures is not possible except under special circumstances. We therefore need to select numerical techniques to evaluate the measures. For Keplerian, circular orbits we have a simple and efficient technique. We know from the solution to Eq. (2.1) that

$$r = a \tag{2.6}$$

For circular orbits we can express the mean anomaly, M, as

$$M = M_0 + \eta t \tag{2.7}$$

where $\eta = \sqrt{\mu/a^3}$ is the mean motion. The position vector in the perifocal system can be written using

$$\mathbf{r}_p = \begin{bmatrix} a\cos M & a\sin M & 0 \end{bmatrix}^T \tag{2.8}$$

To obtain the vector in the inertial system we can apply the rotation matrix

$$\mathbf{R}^{Ip} = \mathbf{R}_3(-\Omega)\mathbf{R}_1(-i)\mathbf{R}_3(-\omega) \tag{2.9}$$

where

$$\mathbf{R}_1(\theta) = \begin{bmatrix} 1 & 0 & 0 \\ 0 & \cos\theta & \sin\theta \\ 0 & -\sin\theta & \cos\theta \end{bmatrix} \tag{2.10}$$

and

$$\mathbf{R}_3(\theta) = \begin{bmatrix} \cos\theta & \sin\theta & 0 \\ -\sin\theta & \cos\theta & 0 \\ 0 & 0 & 1 \end{bmatrix} \tag{2.11}$$

Then we can write $\mathbf{r}_I$ using

$$\mathbf{r}_I = \mathbf{R}^{Ip}\mathbf{r}_p \tag{2.12}$$

For eccentric orbits we must use a more computationally expensive approach. We can solve for the eccentric anomaly E from Kepler's equation

$$M = E - e\sin E \tag{2.13}$$

and solve for ν from

$$\sin\nu = \frac{\sqrt{1-e^2}\sin E}{1 - e\cos E} \tag{2.14}$$

Then the position vector can be written using

$$\mathbf{r}_p = \begin{bmatrix} r\cos\nu & r\sin\nu & 0 \end{bmatrix}^T \tag{2.15}$$

where r is given by

$$r = \frac{a(1-e^2)}{1+e\cos\nu} \tag{2.16}$$

However in this thesis we numerically integrate the two-body equation of motion

$$\ddot{\mathbf{r}} = -\mu\frac{\mathbf{r}}{r^3} \tag{2.17}$$

using a fourth-order Runge-Kutta integrator.

The orbit performance measures developed in Ch. 3 are functions of the angle between two satellites, the distance between two satellites, or the separation area. The separation area algorithm is discussed in Ch. 3. We need to detail how to calculate the angle, α, between two spacecraft and the distance between two spacecraft, d. We can calculate α using the dot product

$$\mathbf{r}_1 \cdot \mathbf{r}_2 = r_1 r_2 \cos\alpha \tag{2.18}$$

and

$$\alpha = \cos^{-1}\left(\frac{\mathbf{r}_1 \cdot \mathbf{r}_2}{r_1 r_2}\right) \tag{2.19}$$

Or using the cross product we have

$$\parallel \mathbf{r}_1 \times \mathbf{r}_2 \parallel = r_1 r_2 \sin\alpha \tag{2.20}$$

and therefore

$$\alpha = \sin^{-1}\left(\frac{\parallel \mathbf{r}_1 \times \mathbf{r}_2 \parallel}{r_1 r_2}\right) \tag{2.21}$$

To evaluate the orbit measure based on inter-satellite distance we can use

$$d = \parallel \mathbf{r}_1 - \mathbf{r}_2 \parallel \tag{2.22}$$

We now have an orbit model to be used in the development of formation performance measures. We also have numerical tools capable of evaluating the measures for both circular and eccentric orbits.

2.4 Summary

To develop performance measures for a distributed array of spacecraft we must use an appropriate model for the orbital dynamics. In general, disturbances from atmospheric drag, third-body effects, and non-spherical gravitation will affect the motion of satellites in formation. However, perturbing forces are difficult to calculate and are not expected to affect preliminary formation design. In this thesis we model the orbital dynamics with Keplerian motion. In general, the orbit performance measures developed in Ch. 3 do not permit a closed-form analytic solution. We must therefore choose efficient numerical algorithms.

In Ch. 3 we review basic remote sensing principles. In light of the requirements of remote sensing missions we develop formation performance measures. Two types of metrics are developed: instantaneous measures that apply to a configuration of spacecraft at given instant, and orbit measures that integrate an instantaneous metric over an orbit.

Chapter 3

Performance Measures

In general due to orbit dynamics there is relative motion between spacecraft in formation over the course of an orbit. Static formations occur only for trivial scenarios. Remote sensing missions use coordinated measurements from multiple spacecraft to obtain higher resolution data. Therefore, the relative motion of spacecraft in formation over the course of an orbit must be appropriate to make the desired observations. In this chapter we develop performance measures that evaluate the effectiveness of the relative motion of spacecraft in formation to allow a comparison of orbit candidates. We can develop performance measures by generalizing classical metrics such as the instantaneous access area for multiple satellite missions, or by developing new measures. We propose two types of measures. Instantaneous metrics such as the generalized access area provide measures of formation effectiveness at a particular instant. Secondly, orbit measures are developed that integrate instantaneous metrics over an orbit period to evaluate the performance of the formation over an orbit.

3.1 Instantaneous Overlap Area

We desire an instantaneous measure of formation effectiveness similar to the access area for single satellite missions. The instantaneous access area (IAA) is defined by Larson and Wertz[17] as all the area that an instrument could potentially see at a given instant. The IAA is defined by the circle on the sphere that defines the Earth's horizon from the point of view of the spacecraft. Hence we call the border of the IAA the horizon circle. Note that the horizon circle is a small circle as opposed to a great circle.[18]

We define a new generalized measure, the instantaneous overlap area (IOA), as the area on the sphere that can be viewed simultaneously by all satellites in formation at the same instant in time. For single satellite missions the access area has upper and lower limiting values and is periodic for Keplerian motion. The lower bound occurs at periapsis when the spacecraft is closest to the Earth, whereas the upper bound occurs at apoapsis when the spacecraft is farthest from the Earth. The instantaneous overlap area is also periodic in time for Keplerian motion; however, the upper and lower bounds exhibit a more complex behavior. When spacecraft are too far apart to have a common viewing area, the overlap area is zero, and therefore the lower limit for the IOA is zero. The instantaneous upper bound is set by the access area of the spacecraft closest to the Earth. For formations in elliptical orbits this value changes over a period due to the changing radii of the orbits.

The size of the overlap area depends on the separation between spacecraft in formation. For formations with small separations the overlap area is large and is on the order of the

instantaneous access area for a single satellite at the same radius. As formation separations increase the overlap area decreases.

There are three configurations of the IOA, each requiring different methods of calculation. The first and simplest configuration occurs when a smaller horizon circle lies completely within a larger horizon circle in a concentric-like configuration as seen in Fig. 3.1. In this case two instantaneous access areas of differing size are in a configuration such that the smaller IAA lies entirely within the larger IAA. The IOA for this configuration is all the area inside the smaller IAA.

Figure 3.1: Concentric-like Overlap Configuration

The second type of overlap area, defined as the double configuration, is defined by the lune of two overlapping circles as seen in Fig. 3.2. A lune is the part of a spherical surface bounded by two overlapping spherical circles. This configuration can occur for formations composed of two satellites as well as for larger formations. For formations of three or more spacecraft this configuration occurs when the overlapping region for two of the circles lies

entirely within the remaining circles. In Fig. 3.2 there are three IAAs however; the border of the IOA is defined by the borders of two of the IAAs. For this scenario the IOA is unchanged if the center IAA is removed.

Figure 3.2: Double Overlap Configuration

The third configuration has a border defined by three or more horizon circles and we call it the multiple boundary configuration. This is the most commonly occurring configuration for a formation involving three or more satellites. A multiple boundary scenario is seen in Fig. 3.3. In this case the IOA is defined by the overlap of three horizon circles. The area for the multiple boundary overlap area is more difficult to calculate than for the concentric and double configurations.

We now develop an algorithm to calculate the overlap area for the three configurations discussed in section 3.1. The overlap area can be calculated knowing the position vectors of all spacecraft in a formation in the same frame of reference at a given instant, and the area that each spacecraft can effectively view. Although an instrument can be pointed at any

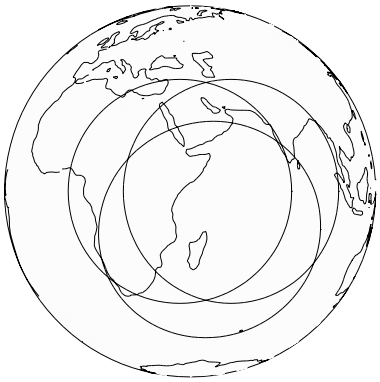

Figure 3.3: Multiple Boundary Overlap Configuration

point within the IAA, the view is distorted near the horizon. We use the minimum elevation angle δ, as seen in Fig 3.4, to define the usable portion of the IAA. The minimum elevation angle is the smallest allowable angle between the line of site and the Earth's surface that permits effective viewing. Hence for non-zero δ the effective horizon is reduced.

We begin by calculating the Earth central angle λ for all n spacecraft in formation. The central angle λ, seen in Fig. 3.4, is defined as the angle between the spacecraft position vector and the outer edge of the effective horizon as seen from the spacecraft.

From the law of sines we have

$$\frac{\sin\lambda}{R_r} = \frac{\sin\left(\pi/2+\delta\right)}{r} \tag{3.1}$$

where R_r is the range from the spacecraft to the outer edge of the effective IAA , and r is the radius of the orbit. From the law of cosines we have

$$R_r^2 = R_e^2 + r^2 - 2R_e r\cos\lambda \tag{3.2}$$

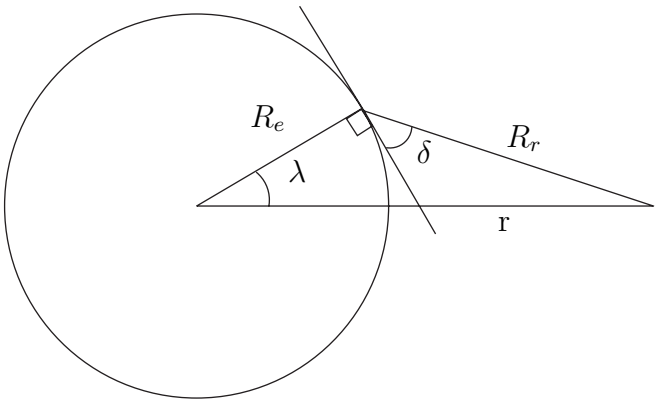

Figure 3.4: Earth-viewing Geometry

where R_e is the radius of the Earth. Solving Eq. (3.1) for R_r and substituting into Eq. (3.2) we obtain

$$\frac{r^2}{\sin^2(\pi/2+\delta)}\sin^2\lambda + 2R_e r\cos\lambda - R_e^2 - r^2 = 0 \tag{3.3}$$

Equation (3.3) cannot be solved explicitly for λ so an iterative scheme such as Newton-Raphson is used.

We now determine all the points of intersection of the horizon circles. A method is developed to calculate the intersection points of two circles with centers defined by the vectors $\mathbf{r}_i$ and $\mathbf{r}_j$ and central angles of λ_i and λ_j. The algorithm is then applied to all pairs in the formation. The centers of the horizon circles are the sub-satellite points. The sub-satellite point is the point where the spacecraft position vector intersects the surface of the Earth. There are two cases in which there are no distinct points of intersection for a pair of horizon circles. The first case occurs for concentric-like configurations as seen in Fig. 3.1. The second case occurs when there is no overlap between a pair of circles. Before attempting

to calculate the intersection points we must first check to see if the pair of circles falls into either of these two categories. To do so we define the angle between two sub-satellite points as β, which can be calculated using

$$\beta_{ij} = \cos^{-1}\left(\frac{\mathbf{r}_i \cdot \mathbf{r}_j}{r_i r_j}\right) \tag{3.4}$$

For two circles with central angles of λ_i and λ_j, and a center-to-center angle of β there is no overlap if

$$\beta > \lambda_i + \lambda_j \tag{3.5}$$

If

$$\beta < \lambda_i + \lambda_j \tag{3.6}$$

then overlap occurs and there may be distinct overlap points. If Eq. (3.6) is satisfied we must determine if a pair of circles are in a concentric-like formation. Assuming $\lambda_j < \lambda_i$ if

$$\beta + \lambda_j > \lambda_i \tag{3.7}$$

then the circles are not in a concentric-like formation and there are distinct overlap points.

The overlap points can be calculated using spherical trigonometry. We apply spherical trigonometric identities that are only valid for triangles defined by great circles so we choose a coordinate system $\mathcal{F}_s$ such that this assumption is satisfied. Choosing an appropriate frame minimizes the use of trigonometric identities and hence provides a more computationally efficient algorithm. The results are rotated into the inertial system $\mathcal{F}_I$ after the application of the trigonometric identities using an appropriate rotation matrix. Frame $\mathcal{F}_s$ is defined

such that the horizon circle with radius λ_j is centered along the x-axis. The y-axis is defined such that the axis of the second horizon circle lies in the x-y plane. The z-axis completes the right-handed triad.

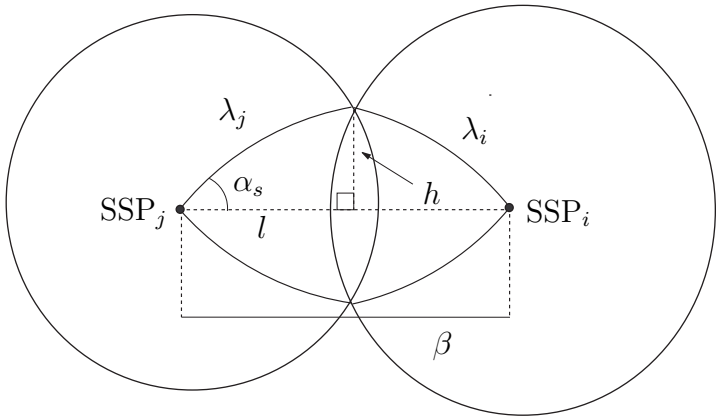

Figure 3.5: Horizon Circle Intersection Geometry

The intersection geometry for two overlapping IAAs is seen in Fig. 3.5. The center-to-center angle, β, and the angular radii of the circles, λ_i and λ_j, are shown. The angles α_s, l, and h are intermediate angles used in the calculation of the intersection points. The angle α_s can be calculated using the law of cosines for oblique spherical triangles:

$$\alpha_s = \cos^{-1}\left(\frac{\cos\lambda_i - \cos\lambda_j\cos\beta}{\sin\lambda_j\sin\beta}\right) \tag{3.8}$$

Using the law of sines for right spherical triangles, we can calculate h and l:

$$h = \sin^{-1}\left(\sin\alpha_s\sin\lambda_j\right) \tag{3.9}$$

$$l = \sin^{-1}\left(\tan h\coth\alpha_s\right) \tag{3.10}$$

Knowing h and l the intersection points in $\mathcal{F}_s$ are

$$\mathbf{i}_{1s} = \begin{bmatrix} \cos h \cos l & \cos h \sin l & \sin h \end{bmatrix}^T \tag{3.11}$$

$$\mathbf{i}_{2s} = \begin{bmatrix} \cos h \cos l & \cos h \sin l & -\sin h \end{bmatrix}^T \tag{3.12}$$

We now determine the rotation matrix to go from frame $\mathcal{F}_s$ to frame $\mathcal{F}_I$. First we express the unit vectors of $\mathcal{F}_s$ in $\mathcal{F}_I$:

$$\hat{\mathbf{i}} = \frac{\mathbf{r}_1}{\| \mathbf{r}_1 \|} \tag{3.13}$$

$$\hat{\mathbf{j}} = \frac{\mathbf{r}_1 \times \mathbf{r}_2}{\| \mathbf{r}_1 \times \mathbf{r}_2 \|} \tag{3.14}$$

$$\hat{\mathbf{k}} = \hat{\mathbf{j}} \times \hat{\mathbf{i}} \tag{3.15}$$

If we express $\hat{\mathbf{i}}$, $\hat{\mathbf{j}}$, and $\hat{\mathbf{k}}$ in column matrix form we can write the rotation matrix from $\mathcal{F}_s$ to $\mathcal{F}_I$ as

$$\mathbf{R}^{is} = \begin{bmatrix} \hat{\mathbf{i}} \mid & \hat{\mathbf{j}} \mid & \hat{\mathbf{k}} \end{bmatrix} \tag{3.16}$$

The inertial representations of the intersection vectors are

$$\mathbf{i}_{1i} = \mathbf{R}^{is} \mathbf{i}_{1s} \tag{3.17}$$

$$\mathbf{i}_{2i} = \mathbf{R}^{is} \mathbf{i}_{2s} \tag{3.18}$$

Applying this technique to all pairs of horizon circles yields all of the intersection vectors in the configuration.

Now we know all of the intersection vectors of the overlapping horizon circles. To calculate the overlap area we must determine which intersection vectors define the common area.

To do so we define the angle β_c as the angle between an arbitrary intersection vector and the i^{th} subsatellite point. By definition the overlap area is the region that can be viewed by all spacecraft simultaneously. Therefore for an intersection vector to define the overlap region it must fall on or within all of the horizon circles. This occurs if

$$\beta_c \leq \lambda_i \tag{3.19}$$

for $1 < i < n$. Applying this criterion to all of the intersection vectors eliminates those that are not involved in the definition of the overlap area.

Knowing all of the intersection vectors defining the IOA and the Earth central angle for each spacecraft we can calculate the overlap area. There are three scenarios that each admits its own method of calculation. The simplest case, seen in Fig. 3.1, occurs when one of the horizon circles is in a concentric-like configuration with all the other circles. This occurs when Eq. (3.6) is satisfied for all pairs of IAAs and Eq. (3.7) is not satisfied. The area is simply the area of the smallest horizon circle:

$$A_o = 2\pi R_e^2(1 - \cos(\lambda_s)) \tag{3.20}$$

where λ_s is the smallest radius of all the horizon circles.

The second case, seen in Fig. 3.2, occurs when only two horizon circles are involved in defining the border of the common area. This occurs for formations composed of only two spacecraft and also for configurations like the one seen in Fig. 3.2. The double configuration occurs when Eqs. (3.6–3.7) are satisfied by all pairs of circles and Eq. (3.19) is satisfied by

two intersection vectors. For this configuration the area can be calculated using

$$\begin{aligned} A_o &= 2\pi R_e^2 - 2R_e^2 \cos\lambda_1 \cos^{-1}\left(\frac{\cos\lambda_2 \cos\lambda_1 \cos\beta}{\sin\lambda_1 \sin\beta}\right) \\ &\quad - 2R_e^2 \cos\lambda_2 \cos^{-1}\left(\frac{\cos\lambda_1 - \cos\lambda_2 \cos\beta}{\sin\lambda_2 \sin\beta}\right) \\ &\quad - 2R_e^2 \cos^{-1}\left(\frac{\cos\beta - \cos\lambda_2 \cos\lambda_1}{\sin\lambda_2 \sin\lambda_1}\right) \end{aligned} \tag{3.21}$$

where λ_1 and λ_2 are the angular radii of the two small circles defining the lune and β is the center-to-center distance.

The third configuration, seen in Fig. 3.3, occurs when the overlap region is defined by three or more horizon circles. This occurs when Eqs. (3.6–3.7) are satisfied by all pairs of circles and Eq. (3.19) is satisfied by three or more intersection vectors. A multiple boundary overlap region is shown in Fig. 3.6. We break the common area into outer and inner regions to permit the application of the appropriate spherical trigonometry relations. We call the shaded grey region the inner area, A_{inner}. The inner area is created by connecting the intersection vectors with great circles. Calculation of A_{inner} is trivial knowing the sum of the interior angles, θ, of the spherical polygon, and the number of points involved, n_p:

$$A_{inner} = \theta - (n_p - 2)\pi \tag{3.22}$$

The outer area is composed of n_p lunes created by the small circles and the great circles defining the inner area. Therefore the area of each lune A_{lune} can be calculated from Eq. (3.21) with one of the angular radii set to 90°. Setting $\lambda_1 = 90°$ and letting λ_2 and β be

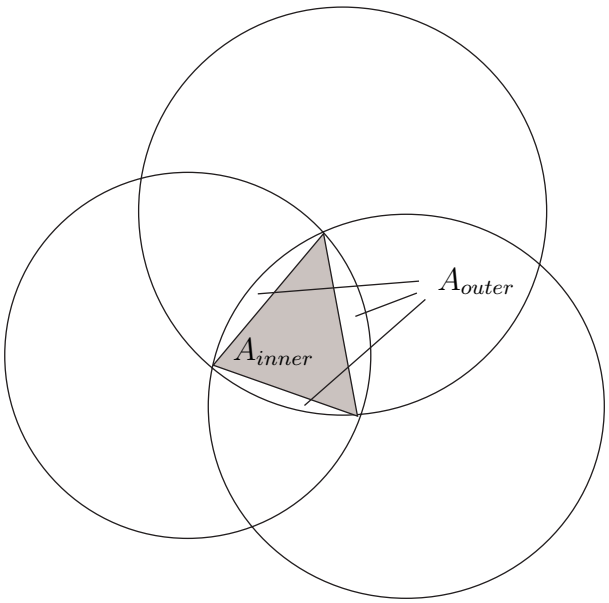

Figure 3.6: Inner/Outer Overlap Area

the angular radii and the center-to-center distance, respectively, the area of a lune is

$$\begin{aligned} A_{lune} &= 2\pi R_e^2 - 2R_e^2 \cos\lambda_2 \cos^{-1}\left(\frac{-\cos\lambda_2 \cos\beta}{\sin\lambda_2 \sin\beta}\right) \\ &\quad - 2R_e^2 \cos^{-1}\left(\frac{\cos\beta}{\sin\lambda_2}\right) \end{aligned} \tag{3.23}$$

The total area of the outer region A_{outer} is obtained by summing the area of each of the lunes calculated from Eq. (3.23) and the total overlap area is obtained from

$$A_o = A_{outer} + A_{inner} \tag{3.24}$$

We now have the tools to calculate the IOA for a distributed array of spacecraft. The IOA provides a measure of "closeness" for spacecraft flying in formation. The value of the IOA is the area on the sphere that all satellites in formation can view simultaneously. Highly separated formations will result in a small IOA while close formations will have large values

Figure 3.7: The Separation Area

for the IOA. We now develop an area measure that indicates the "separation" of a formation of spacecraft.

3.2 Instantaneous Separation Area

The IOA provides a measure of "closeness" between spacecraft in formation. A measure of the "separation" between spacecraft in a formation is also useful. We define the instantaneous separation area (ISA) as the region enclosed by connecting the outermost sub-satellite points with great circles. The ISA is shown for an arbitrary configuration in Fig. 3.7. For this case four overlapping IAAs compose the IOA. The subsatellite points are connected to form the diamond-shaped ISA in the middle of the IOA.

The ISA is directly proportional to the separation between spacecraft in the formation. For formations with small separations the separation area is be small. As separations increase

the separation area also increases.

For formations composed of more than three spacecraft we must carefully define what is meant by the "outermost" sub-satellite point. An arbitrary configuration of subsatellite points is seen in Fig. 3.8. The rotation angles θ_b and θ_c are shown for points b and c, respectively. In general, given three points a$'$, a, and b, the rotation angle of a$'$ to b about point a is the angle through which the line segment ab is rotated away from line segment aa$'$. Given the line segments ab and ac, we define the "outermost" point to be the one that results in the smallest rotation angle. In this case the outermost point is b because $\theta_b < \theta_c$.

Calculation of the separation area is simpler than for the overlap area because its borders are defined by great circles. Once the border is determined, the sum of the interior angles can be calculated using simple trigonometric relations and the area can be calculated from Eq. (3.22).

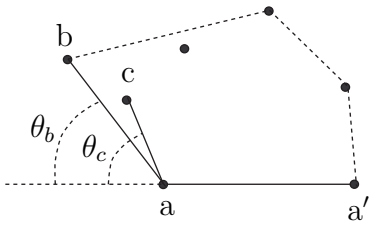

Figure 3.8: Outermost Sub-Satellite Point

The IOA and the ISA provide two measures of instantaneous performance for a formation of spacecraft. However, we need to develop metrics that investigate the effectiveness of the relative positions of spacecraft over an orbit in light of the separations required to perform

remote sensing missions. In section 3.3 we investigate some basic remote sensing concepts. We then proceed to develop orbit performance measures that evaluate a formation's ability to perform remote sensing missions.

3.3 Distributed Sensors Concept

The formation flying spacecraft concept affords new possibilities for space-based remote sensing missions. The primary advantage of a distributed array of spacecraft is the difference in perspective provided by different satellites in the array. In Fig. 3.9 we see two spacecraft whose positions are defined by $\mathbf{r}_1$ and $\mathbf{r}_2$. The separation of the spacecraft is defined by the distance d and the angle α. The light grey shaded areas are the cones defining the field of view for each spacecraft. The common viewing region is shaded dark grey. Both spacecraft have an instrument looking at a common target defined by $\mathbf{r}_t$ on the Earth's surface. The range vectors $\mathbf{t}_1$ and $\mathbf{t}_2$ define the target line-of-sight for each spacecraft. We call the angle between range vectors the perspective angle, α_p.

The perspective angle is the angle of interest in remote sensing missions involving interferometry or stereographic viewing. Through the use of stereographic viewing techniques, the angle α_p allows the calculation of depth information unobtainable from single source data. Similarly, the distance d increases the effective aperture size of two sensing instruments through the techniques of interferometry. Therefore to evaluate formation performance, we need to determine if the relative positions of the spacecraft in formation permit an appro-

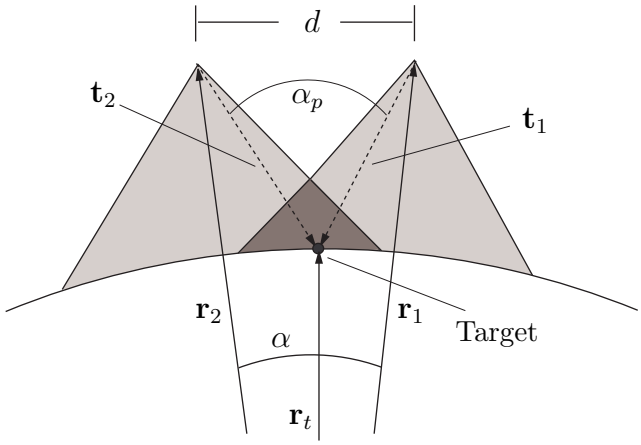

Figure 3.9: Remote Sensing Geometry

priate range of α_p for a given mission. Although we do not derive the exact relation here, we know from inspection of Fig. 3.9 that

$$\alpha_p = f(\mathbf{r}_1, \mathbf{r}_2, \mathbf{r}_t) \tag{3.25}$$

We also know from inspection that

$$\alpha = f(\mathbf{r}_1, \mathbf{r}_2) \tag{3.26}$$

and

$$d = f(\mathbf{r}_1, \mathbf{r}_2) \tag{3.27}$$

We argue that we can perform an *a priori* analysis to determine the range of α or d that will provide an acceptable range of α_p for a given mission. With this assumption we can determine the ability of a formation to perform stereographic or interferometric missions by investigating the inter-satellite distances or angular separations. We can also argue that for desired inter-satellite separations based on d or α, there exists a characteristic value

of the instantaneous overlap area and separation area. For example, suppose we desire inter-satellite separations of 1000 m. For a four-spacecraft formation with separations near 1000 m the separation area is on the order of 1×10^6 m^2. By requiring the separation area to remain near 1×10^6 m^2 throughout an orbit we constrain the spatial separations to be on the order of 1000 m. Therefore we can use the IOA and the separation area to determine effective spacecraft array configurations. With these considerations, we can develop orbit performance measures that allow an investigation into the ability of a formation to perform a remote sensing mission effectively.

3.4 Orbit Performance Measures

In addition to the instantaneous performance measures, we also desire metrics that allow an evaluation of the orbits composing a formation. We develop a strategy that integrates an instantaneous measure over an orbit period. The instantaneous measures are based on inter-satellite distances, angular separations, and the ISA measure. This technique allows the evaluation of the relative motion between spacecraft over an orbit period. The general form for the orbit performance measures is

$$W = \frac{1}{T} \int_0^T f(\mathbf{r}_1, \mathbf{r}_2, ..., \mathbf{r}_n)\, dt \tag{3.28}$$

The primary difference between the different orbit measures is the instantaneous relative position metric, $f(\mathbf{r}_1, \mathbf{r}_2, ..., \mathbf{r}_n)$.

3.4.1 Angular Separation Orbit Measure

In section 3.3 we conclude that we can assess the ability of a formation to perform specific remote sensing missions by investigating the angular separations or distances between the spacecraft over an orbit period. We wish to ensure that separations in a formation are appropriate to perform a desired mission. We propose an instantaneous measure of the form

$$f_\alpha = \frac{1}{\eta_s T} \sum_{i=1}^{n-1} \sum_{j=i+1}^{n} w_\alpha(\alpha_{ij}) \tag{3.29}$$

where n is the number of spacecraft in the array, α_{ij} is the angular separation between the i^{th} and j^{th} satellites, and η_s is the number of distinct angles in the formation:

$$\eta_s = \frac{n^2 - n}{2} \tag{3.30}$$

The weight w_α is evaluated for each unique angle, α_{ij}, in the formation at a given instant. The individual weight values are added together and normalized on η_s. By normalizing on η_s we ensure that the maximum instantaneous weight function is one. The specific form of w_α is chosen according to the necessary angular separations to meet mission requirements.

We consider two forms for w_α as seen in Fig. 3.10. For both functions, $w_{max} = 1$ occurs at angular separations resulting in spatial separations of 3 km at a radius of 8000 km. The first function is a quartic polynomial which does not apply a negative weight for formations outside the allowed angular separation limit. The second function is parabolic and applies a negative weight for formations with unacceptable angular separations. We discuss the forms of w_α more thoroughly in section 4.1.

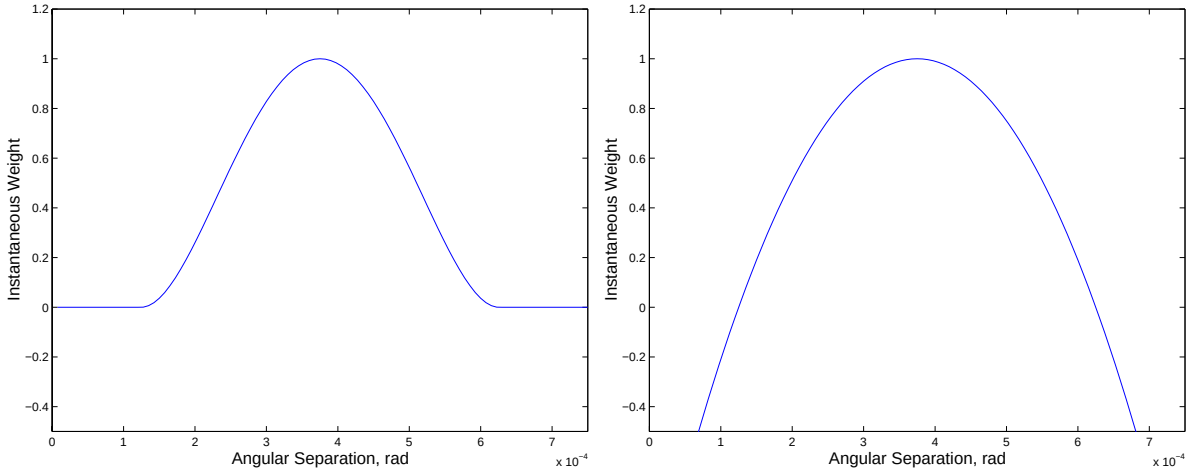

Figure 3.10: Empirical Functions, w_α

Recalling the general form for the orbit measures seen in Eq. (3.28) we can substitute Eq. (3.29) to obtain the orbit performance measure W_α:

$$W_\alpha = \frac{1}{\eta_s T} \int_0^T \sum_{i=1}^{n-1} \sum_{j=i+1}^{n} w_\alpha(\alpha_{ij}) \tag{3.31}$$

We now have an orbit performance measure based on the angular separations between spacecraft in a distributed array. We can also assess orbit performance using a function based on the distance between spacecraft.

3.4.2 Distance-Based Orbit Measure

We propose a new instantaneous metric, f_d, based on the distances between satellites in formation

$$f_d = \frac{1}{\eta_s T} \sum_{i=1}^{n-1} \sum_{j=i+1}^{n} w_d(d_{ij}) \tag{3.32}$$

where d_{ij} is the distance between the i^{th} and j^{th} satellites. The form of f_d is the same as the form of f_α; however, the independent variable is different. The weight w_d is evaluated for each unique distance, d_{ij}, in the formation at a given instant. The individual weight values are added together and normalized on η_s. The specific form of w_d is chosen according to the necessary spatial separations to meet mission requirements.

We consider a parabolic form for w_d as seen in Fig. 3.11. The maximum for w_d occurs for a separation of 3000 m. The upper and lower limits of w_d are 5000 m and 1000 m respectively. We discuss the form of w_d more thoroughly in section 4.1.

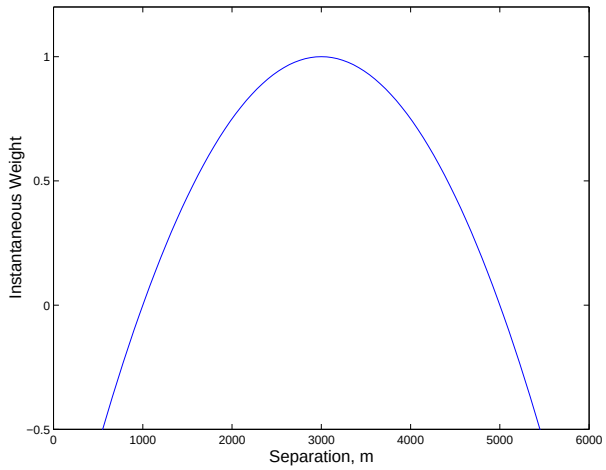

Figure 3.11: Empirical Function, w_d

Recalling the general form for the orbit measures seen in Eq. (3.28) we can substitute Eq. (3.32) to obtain the orbit performance measure W_d:

$$W_d = \frac{1}{\eta_s T} \int_0^T \sum_{i=1}^{n-1} \sum_{j=i+1}^{n} w_d(d_{ij})\, dt \tag{3.33}$$

We now have a second orbit performance measure based on the inter-satellite distances

of a distributed array of spacecraft. We can argue that for desired inter-satellite separations based on d or α, there exists a characteristic value of the instantaneous separation area. With this assumption, we can develop another orbit performance measure based on the ISA.

3.4.3 Weighted Separation Area Orbit Measure

We develop a third orbit metric based on the instantaneous separation area. This measure is applicable to formations composed of more than two spacecraft because for two-spacecraft scenarios the separation area is undefined. By applying a weight function to the separation area we can penalize formations whose separation area is either too large or too small. By integrating the weight of the separation area over an orbit we obtain a measure of orbit performance. Specifically

$$W_A = \frac{1}{T}\int_0^T w_A(A_s)\, dt \tag{3.34}$$

We consider a parabolic form for w_A seen in Fig. 3.12. The ideal separation area occurs at 2×10^6 m^2. Allowable separations occur between 1×10^6 m^2 and 3×10^6 m^2. These separation area values are representative for separations defined by w_d seen in Fig. 3.11. Configurations outside of this range receive a negative weight.

For the rest of the analysis we use the notation seen in sections 3.4.1–3.4.3 to distinguish between an orbit performance measure and an instantaneous weight function. An upper-case W denotes an orbit performance measure. The subscript α, d, or A distinguishes the angular, distance, and separation area measures respectively. A lower-case w denotes an

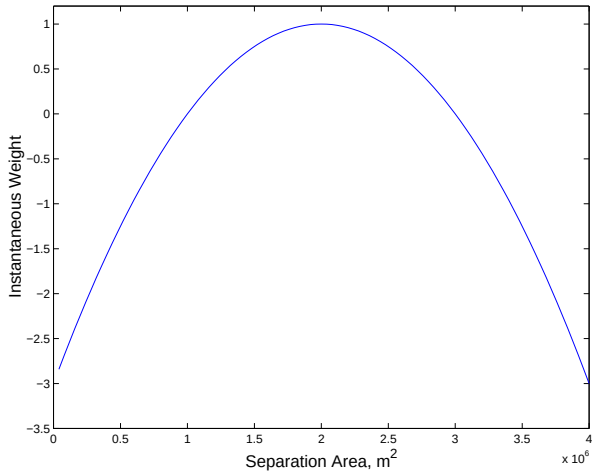

Figure 3.12: Empirical Function, w_A

instantaneous weight function. The subscript for w describes the type of weight, whether it is parabolic, p, quartic, q, or an area weight A.

We now have three orbit performance measures that allow the assessment of the separations of spacecraft in formation over a Keplerian orbit. The angular separation measure, W_α, integrates over an orbit period the summation of an instantaneous angular separation metric. The distance measure, W_d, has the same form but uses a distance-based instantaneous separation metric. Finally, the area-based measure, W_A, integrates over one period an instantaneous weight based on the ISA.

3.5 Summary

In general, due to orbit dynamics there is relative motion between spacecraft in formation over the course of an orbit. Remote sensing missions use coordinated measurements from

multiple spacecraft in formation to obtain higher resolution data. Therefore, the relative motion of spacecraft in formation over the course of an orbit must be appropriate to perform the desired observations. We desire performance metrics that allow the assessment of the ability of a distributed array of spacecraft to meet mission requirements. Two types of measures are proposed in this thesis. Instantaneous measures such as the overlap area and the separation area provide measures of formation effectiveness at a particular instant. Orbit metrics are developed that integrate instantaneous measures over an orbit period to evaluate the performance of the formation over an orbit. The orbit performance measures involve angular separation of spacecraft, the distance between spacecraft, and the instantaneous separation area. In Chs. 4–5 we apply the measures to two different formations. We determine optimum configurations for each formation and characterize the effects of changes in formation parameters on the performance measures.

Chapter 4

The Diamond Formation

In Ch. 3 we develop orbit performance measures based on the integration of an instantaneous metric over one orbit. The measures involve the angular separation of spacecraft, the distance between spacecraft, and the instantaneous separation area. In this chapter we use the orbit model developed in Ch. 2 to develop a formation we call the diamond formation. We apply the orbit performance measures to the diamond formation to determine optimal configurations. We also investigate the effects of changing orbit parameters such as inclination, semimajor axis, and eccentricity on the performance measures. When appropriate we use simplifying assumptions to obtain a simple preliminary analysis and then look at more complex models.

4.1 Development of the Diamond Formation

We now develop a formation we call the diamond formation. A picture of the diamond formation is seen in Fig. 4.1. The relative positions of the satellites at a given instant form a diamond-like shape. To ensure a cohesive, formation all of the orbits have the same semimajor axis. Two of the spacecraft, labeled 1 and 3, are in circular, coplanar orbits. The angular separation between the coplanar spacecraft is defined as the longitudinal separation, δ_{lon}. The dimension δ_{lon} remains constant over an orbit. The remaining two spacecraft, labeled 2 and 4, are in orbits inclined at equal amounts with respect to the coplanar orbits and their ascending nodes are placed 180° apart. At the initial epoch spacecraft 2 and 4 are

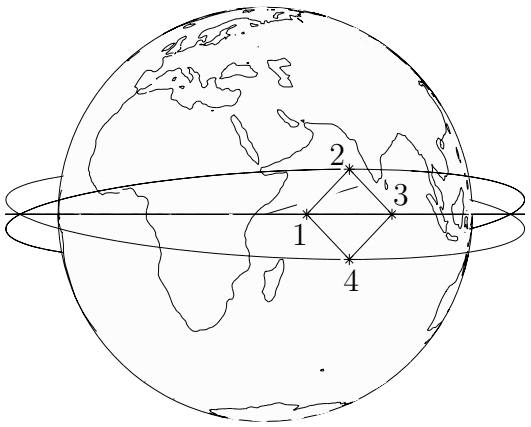

Figure 4.1: The Diamond Formation

at their maximum declination with respect to the coplanar orbits and lie midway in longitude between the two equatorial spacecraft. The initial angular separation between spacecraft 2 and 4 is defined as the latitudinal separation, δ_{lat}. As the orbits evolve over one period the

diamond shape will open and close due to the relative motion of spacecraft in the inclined orbits.

The diamond formation is defined by the two independent variables, δ_{lon} and δ_{lat}. All of the orbital elements for the formation can be written in terms of these two variables. The performance measures developed in Ch. 3 are only dependent on the relative motion of the spacecraft. Therefore, we can develop a set of orbital elements for the diamond formation without concern for the motion with respect to specific targets on the Earth. The orbital element sets we have chosen are seen in Table 4.1.

Table 4.1: Orbital Elements for the Diamond Formation

Orbit #	a	e	i	ω	Ω	ν	u	ℓ
1	a	0	0	undef.	undef.	undef.	undef.	0
2	a	0	$\delta_{lat}/2$	undef.	$(\pi + \delta_{lon})/2$	undef.	$3\pi/2$	$2\pi + \delta_{lon}/2$
3	a	0	0	undef.	undef.	undef.	undef.	δ_{lon}
4	a	0	$\delta_{lat}/2$	undef.	$(3\pi + \delta_{lon})/2$	undef.	$\pi/2$	$2\pi + \delta_{lon}/2$

The quantities δ_{lon} and δ_{lat} are angular separations between spacecraft in radians. For close formations such as those considered in this thesis the angular separation between spacecraft is on the order of 10^{-4} rad. To provide a more intuitive understanding, the results of the orbit performance measures are often presented in meters. This is to say that the quantities δ_{lon} and δ_{lat} are converted to a distance at the radius appropriate for the given problem. In this case we use the notation d_{lon} and d_{lat} to represent the spatial separation.

We now investigate the results of applying the performance measures developed in Ch. 3 to the diamond formation. We wish to evaluate the performance of a formation by integrating an instantaneous weight function over a Keplerian orbit. Recall we have the general form

$$W = \frac{1}{T}\int_0^T f(\mathbf{r}_1, \mathbf{r}_2, ..., \mathbf{r}_n)\, dt \tag{4.1}$$

For the diamond formation we can investigate the effect of the initial state on the performance using graphical techniques because it is defined by only two state variables.

4.2 Angular Measure

The angular performance measure W_α developed in Ch. 3 attempts to ascertain the effectiveness of the orbits by investigating the angular separation between spacecraft in formation over an orbit. The general form of the angular measure is

$$W_\alpha = \frac{1}{\eta_s T}\int_0^T \sum_{i=1}^{n-1}\sum_{j=i+1}^{n} w_\alpha(\alpha_{ij})\, dt \tag{4.2}$$

where $w_\alpha(\alpha_{ij})$ is chosen by the analyst. Two forms for $w_\alpha(\alpha_{ij})$ are considered in this thesis. We first investigate a quartic form, then we assume a quadratic form.

4.2.1 Quartic Instantaneous Weight

We first investigate a quartic form for w_α such that

$$w_q = \begin{cases} 0 & \alpha < \alpha_l \\ (\alpha_{ij} - \alpha_l)^2(\alpha_{ij} - \alpha_u)^2/\alpha_s & \alpha_l < \alpha < \alpha_u \\ 0 & \alpha > \alpha_u \end{cases} \tag{4.3}$$

where

$$\alpha_l = 1.25 \times 10^{-4}\text{rad} \qquad \alpha_u = 6.25 \times 10^{-4}\text{rad} \qquad \alpha_s = 3.90625 \times 10^{-15}\text{rad} \tag{4.4}$$

A graphical representation of the quartic weight function can be seen in Fig. 3.10. The angles α_l and α_u are the upper and lower limits on angular separations, respectively. We have chosen α_l so that the lower limit on distance separations is 1 km at a radius of 8000 km. The upper angular limit is chosen so that the maximum distance separation is 5 km at a radius of 8000 km. The limits are chosen to ensure a close formation with separations on the order of a few kilometers and an optimum separation of 3 km. We divide by the normalization factor α_s to ensure w_q has a maximum value of one. A quartic instantaneous weight is chosen to ensure a smooth function. If a parabolic weight function is chosen, and the condition $w = 0$ for $\alpha < \alpha_l$ and $\alpha > \alpha_u$ is applied, then w_q will not be smooth and difficulties will result in the application of optimization schemes.

Figure 4.2 shows the surface plot generated from the application of W_α using the quartic instantaneous weight function w_q. The maximum value is $W_{\alpha_{max}} = 0.7558$ which occurs for a longitudinal separation of 5500 m and a latitudinal separation of 3500 m. The instantaneous

weight function w_q is zero for all angles resulting in spatial separations of less than 1 km. The performance measure is zero for those initial conditions that result in spatial separations that are always less than 1 km. The longitudinal separation has a larger effect on the performance than the latitudinal separation. If the initial longitude is poor according to w_q it remains so throughout the orbit and does not contribute to the performance. The latitudinal separation has a different effect on performance due to the oscillatory motion of spacecraft 2 and 4. If δ_{lon} is large and falls outside of the acceptable separation range there is still a contribution to the performance over the orbit. This contribution is due to the fact that over an orbit δ_{lon} begins at the initial value, goes to zero, and then increases back to the original value. In doing so the angular separation between spacecraft 2 and 4 must pass through the acceptable range of angular separation and positively contribute to the performance.

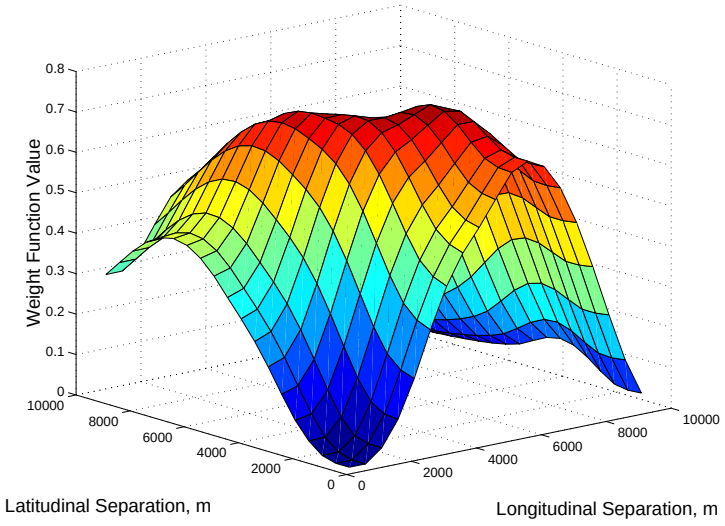

Figure 4.2: W_α with Quartic Instantaneous Weight

4.2.2 Parabolic Instantaneous Weight

The quartic weight function of Eq. (4.3) does not apply a penalty to configurations that result in unacceptable angular separations. A parabolic form for w however would penalize a formation for unacceptable configurations. We now investigate applying an instantaneous weight of the form

$$w_p = (\alpha_{ij} - \alpha_u)(\alpha_{ij} - \alpha_u)/\alpha_s \tag{4.5}$$

where

$$\alpha_l = 1.25 \times 10^{-4}\text{rad} \qquad \alpha_u = 6.25 \times 10^{-4}\text{rad} \qquad \alpha_s = -6.25 \times 10^{-8}\text{rad} \tag{4.6}$$

to the diamond formation. A graphical representation of the parabolic weight function can be seen in Fig. 3.10. The upper and lower limits are the same as for the quartic case. We have chosen α_l so that the lower limit on distance separations is 1 km at a radius of 8000 km. The upper angular limit is chosen so that the maximum distance separation is 5 km at a radius of 8000 km. The limits are chosen to ensure a close formation with separations on the order of a few kilometers and an optimum separation of 3000 m. We divide by the normalization factor α_s to ensure that the maximum value of w_p is $w_p = 1$.

Application of the W_α performance measure with the parabolic weight function is presented in Fig. 4.3. The maximum value $W_{\alpha_{max}}$, is 0.8198 and occurs at a longitudinal separation of 4000 m and a latitudinal separation of 4500 m. The effects of latitudinal and longitudinal separation on the parabolic case are similar to those obtained using the quartic weight function. The longitudinal separation has a larger effect on the performance. The

surface is smoother for the parabolic case than for the quartic weight function case. This smoothness is primarily due to the negative weight imposed by the parabolic function for separations that do not fall within the acceptable range.

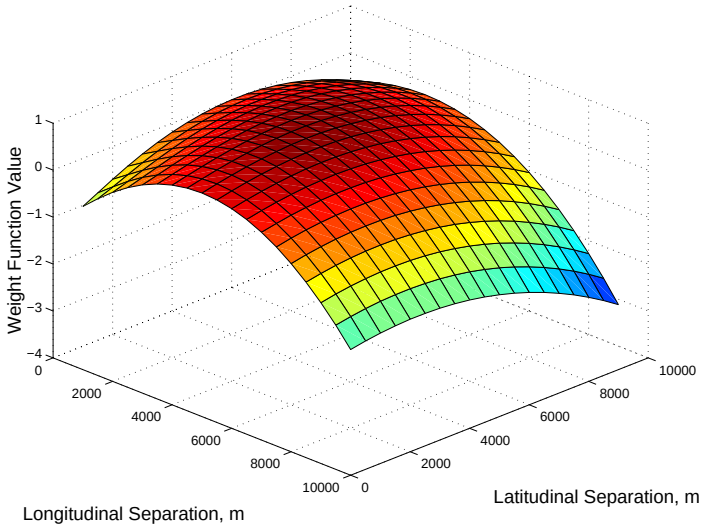

Figure 4.3: W_α with Parabolic Instantaneous Weight

The Effects of Changing Semimajor Axis

In sections 4.2.1–4.2.2 we hold a fixed at 8000 km and evaluate W_α for different configurations of the diamond formation. However, the effect of changing the semimajor axis on formation performance is important. We now determine the effects of changing the semimajor axis of the formation on the orbit measure W_α. Hence we wish to evaluate the derivative

$$\frac{\partial W_\alpha}{\partial a} = \frac{1}{\eta_s T} \int_0^T \sum_{i=1}^{n-1} \sum_{j=i+1}^{n} \frac{\partial}{\partial a} w_\alpha(\alpha_{ij})\, dt \tag{4.7}$$

To determine $\partial W_\alpha/\partial a$ we must determine the derivative of the instantaneous weight function $\partial w_\alpha/\partial a$. In general, the parabolic weight function w_p has the form

$$w_p = c_1\,\alpha_{ij}^2 + c_2\,\alpha_{ij} + c_3 \tag{4.8}$$

so the derivative of w_p with respect to a is

$$\frac{\partial w_p}{\partial a} = 2c_1\,\alpha_{ij}\frac{\partial \alpha_{ij}}{\partial a} + c_2\,\frac{\partial \alpha_{ij}}{\partial a} \tag{4.9}$$

The problem of determining $\partial W_\alpha/\partial a$ reduces to finding the derivative of α_{ij} with respect to a where we know α_{ij} from

$$\alpha_{ij} = \cos^{-1}\left(\frac{\mathbf{r}_1 \cdot \mathbf{r}_2}{r_1 r_2}\right) \tag{4.10}$$

We can rewrite Eq. (4.10) as

$$\alpha_{ij} = \cos^{-1}\left(\hat{\mathbf{r}}_1 \cdot \hat{\mathbf{r}}_2\right) \tag{4.11}$$

where $\hat{\mathbf{r}}_1$ and $\hat{\mathbf{r}}_1$ are unit vectors in the $\mathbf{r}_1$ and $\mathbf{r}_1$ directions respectively. For a given instant in time, a change in a does not affect the unit vectors $\hat{\mathbf{r}}_1$ and $\hat{\mathbf{r}}_2$. Hence we can write

$$\frac{\partial \alpha_{ij}}{\partial a} = 0 \tag{4.12}$$

Substituting Eq. (4.12) into Eq. (4.9) we see that

$$\frac{\partial w_p}{\partial a} = 0 \tag{4.13}$$

Substituting this result into Eq. (4.7) shows that W_α is not dependent on a:

$$\frac{\partial W_\alpha}{\partial a} = 0 \tag{4.14}$$

The same results are obtained for the quartic instantaneous weight function of Eq. (4.3) because

$$\alpha_{ij} \neq f(a) \tag{4.15}$$

We have shown that changes in a do not affect W_α. The effect of changing eccentricity on W_α is also important. We now determine the effect of changing eccentricity on the performance of the diamond formation using the angular orbit performance measure.

The Effect of Changing Eccentricity

The effect of changes in eccentricity on W_α is important for several reasons. Improvements in performance might be possible by allowing the eccentricity to vary. The effect of small yet non-zero eccentricity values on performance is important because in reality no orbit is perfectly circular. Determining the effects of eccentricity on W_α analytically is non-trivial. Therefore, we investigate the results of evaluating W_α over a range of eccentricities.

Plots of W_α with the quartic weight for a range of eccentricities are shown in Figs. 4.4–4.6. We assume all orbits have the same eccentricity in order to simplify the analysis. For a nominal value of $e = 0.00001$ there is a small negative effect on the performance of the formation. The maximum for W_α drops from 0.75 to 0.74. Increasing the eccentricity to 0.00005 further reduces the maximum performance to 0.6707. A large change in the performance occurs for $e = 0.0001$. The optimum value for W_α drops to 0.59. However, the performance improves for certain initial conditions. As eccentricity is further increased to

0.00015 the optimum value of W_α decreases to 0.51.

We see for the quartic weight there is a decreasing trend in W_α for increasing values of eccentricity. This occurs even for small values of e. This could be of concern operationally because the range of eccentricities considered here is on the order of the eccentricity of actual orbits considered circular in operating missions.

In Figs. 4.7–4.9, W_α is plotted using the parabolic weight for a range of eccentricity values. The shape of the plots is qualitatively similar for $e = 0$ and $e = 0.00001$, and the optimum values are 0.8198 and 0.8179 respectively. A larger decrease in performance is seen for $e = 0.0005$. The maximum is reduced to 0.7320. A dramatic decrease in performance occurs for $e = 0.0001$ and $e = 0.00015$. The maximum in performance for $e = 0.00015$ is W_α =-0.2372 suggesting an extremely poor formation. A downward trend in performance is also seen for the quartic instantaneous weight function. This suggests that the performance of the diamond formation is extremely sensitive to small changes in eccentricity. Therefore, for the best results the eccentricity of the orbits in the diamond formation should be kept as close to zero as possible.

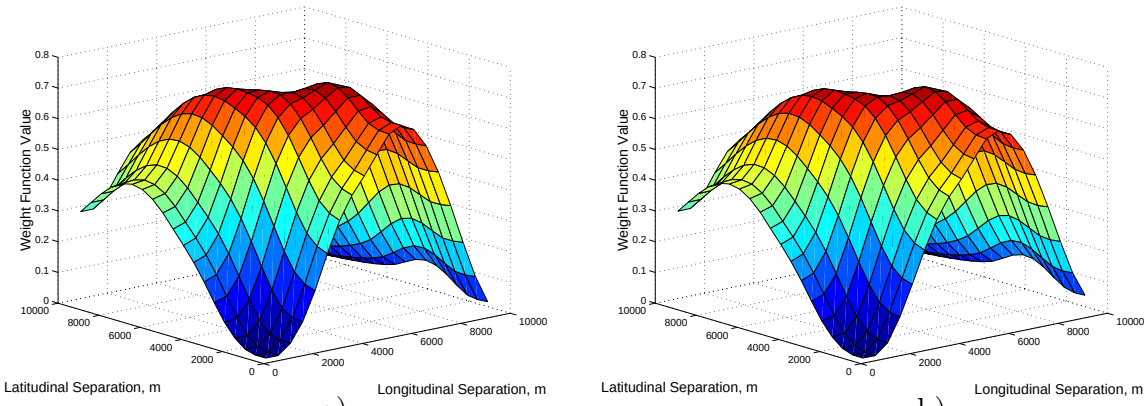

Figure 4.4: W_α with Quartic Weight: a) $e = 0$; b) $e = 0.00001$

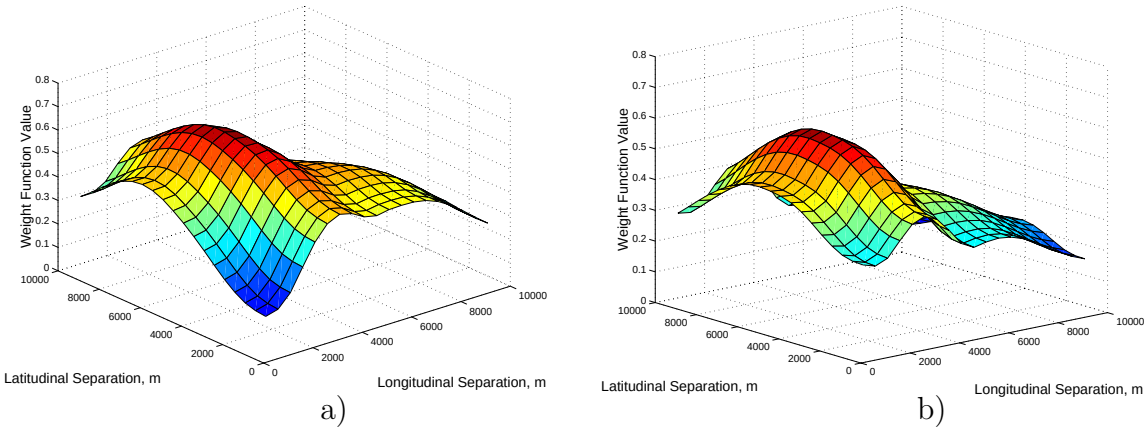

Figure 4.5: W_α with Quartic Weight: a) $e = 0.00005$; b) $e = 0.0001$

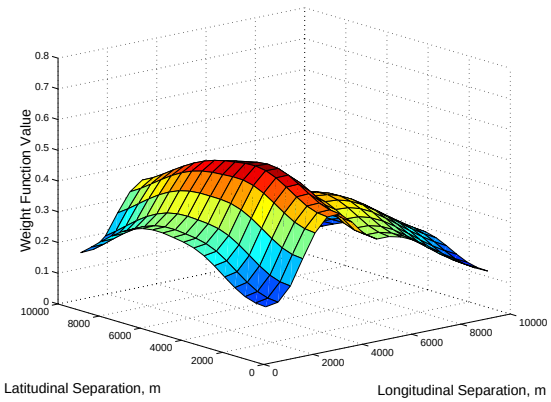

Figure 4.6: W_α with Quartic Weight for $e = 0.00015$

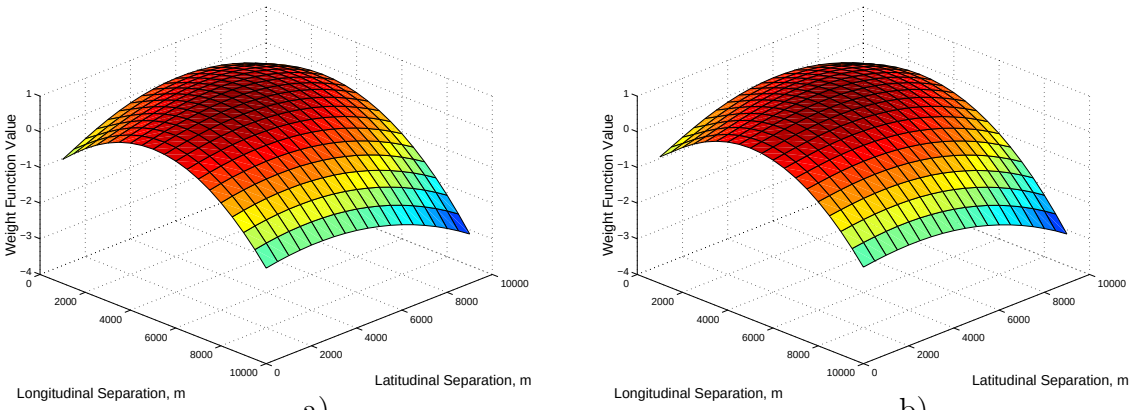

Figure 4.7: W_α with Parabolic Weight: a) $e = 0$; b) $e = 0.00001$

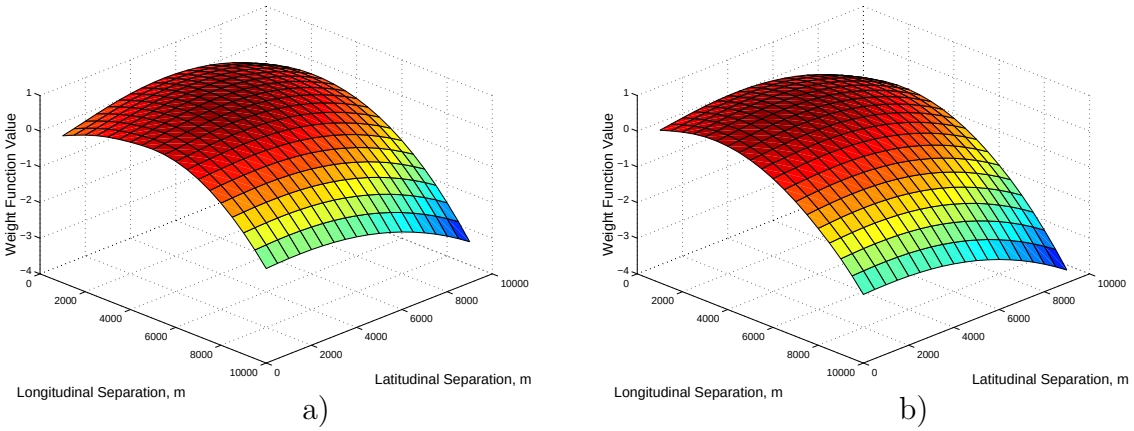

Figure 4.8: W_α with Parabolic Weight: a) $e = 0.00005$; b) $e = 0.0001$

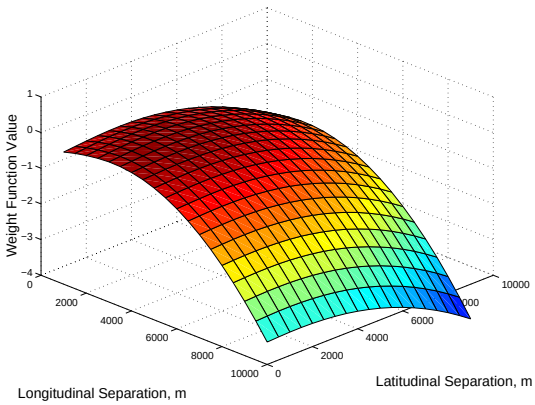

Figure 4.9: W_α with Parabolic Weight for $e = 0.00015$

4.3 Distance Measure

The second measure uses the inter-satellite distance in place of the angular separation in the instantaneous weight function. The general form is

$$W_d = \frac{1}{\eta_s T} \int_0^T \sum_{i=1}^{n-1} \sum_{j=i+1}^{n} w_d(d_{ij})\, dt \tag{4.16}$$

We assume a parabolic form for $w_d(d_{ij})$ where

$$w_d = (d - d_l)(d - d_u)/d_n \tag{4.17}$$

and

$$d_l = 1000 \text{ m} \qquad d_u = 5000 \text{ m} \qquad d_n = -4000000 \text{ m}^2 \tag{4.18}$$

A graphic representation of the distance weight function can be seen in Fig. 3.11. The maximum in w_d occurs at separations of 3000 m. The upper bound, d_u, occurs at 5000 m and the lower bound, d_l, occurs at 1000 m. The normalization factor, d_n, assures that the maximum value of $w_d = 1$.

The application of W_d to the diamond formation is shown in Fig. 4.10. The measure is applied to two formations differing only in semimajor axis. On the left are the results for $a = 8000$ km. The results for $a = 10000$ km are on the right. For $a = 8000$ km the optimum is 0.8198. The optimum occurs at $d_{lon} = 4000$ m and $d_{lat} = 4500$ m. This is the same as the optimum obtained from the angular measure W_α with the parabolic weight. Both W_α and W_d find the same optimum because the parabolic distance weight is chosen to be consistent

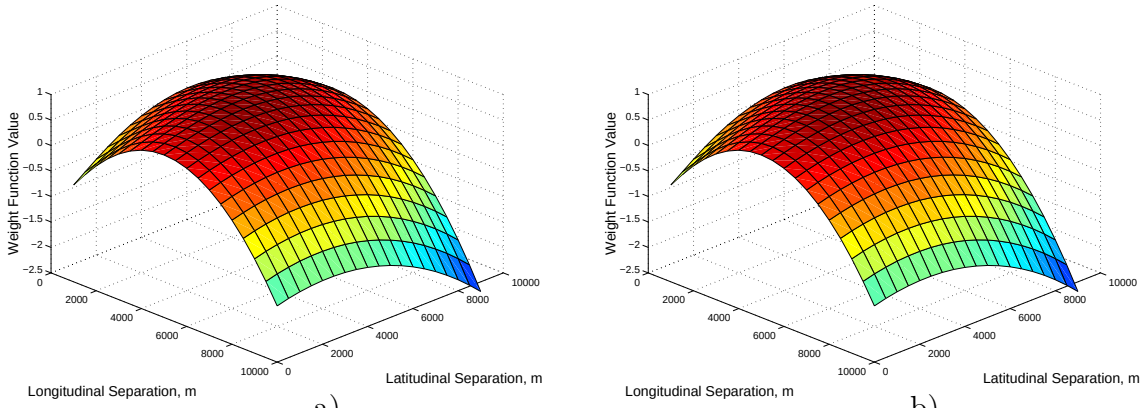

Figure 4.10: W_d for Two Values of Semimajor Axis: a) $a = 8000$ km ; b) $a = 10{,}000$ km

with the parabolic angular measure. Specifically, the optimum value of w_d is chosen to be 3 km. The optimum w_α results in a separation of 3 km at a radius of 8000 km.

4.3.1 The Effects of Changing the Semimajor Axis

The results of W_d for $a = 8000$ km and $a = 10000$ km shown in Fig. 4.10 appear the same. This suggests that W_d is independent of the semimajor axis which at first seems counterintuitive. However, if the instantaneous weight function

$$w_d = c_1 d^2 + c_2 d + c_3 \tag{4.19}$$

is considered, an explanation can be obtained. By defining a formation with the same longitudinal and latitudinal separation at a new semimajor axis, we change the period of the relative motion over an orbit. If the time for each formation is normalized by its corresponding period, the relative motion solution is nearly the same for small e. Hence the formation with a greater a has a longer period than the formation with a smaller a. However, the

relative motion is nearly the same and therefore W_d has a similar solution for both values of the semimajor axis.

4.3.2 The Effects of Changing Eccentricity

Plots of W_d for a range of eccentricities are shown in Figs. 4.11–4.13. There are five plots with eccentricities varying between 0 and 0.00015. In general, increasing e results in a flattening effect on the surfaces. As e increases the curves are shifted downward. The plots are qualitatively similar to those for W_α with the parabolic shown in Figs. 4.7–4.9. A downward trend in performance is seen for increasing e. For $e = 0$ the maximum in W_d is 0.8197. Increasing e to 0.00001 results in a small decrease in the maximum to 0.8188. A dramatic reduction in performance occurs when e is raised to 0.00015. The new maximum in W_d is -0.2152 suggesting an extremely poor configuration. Like W_α, the distance measure indicates that the performance of the diamond formation is sensitive to small changes in eccentricity.

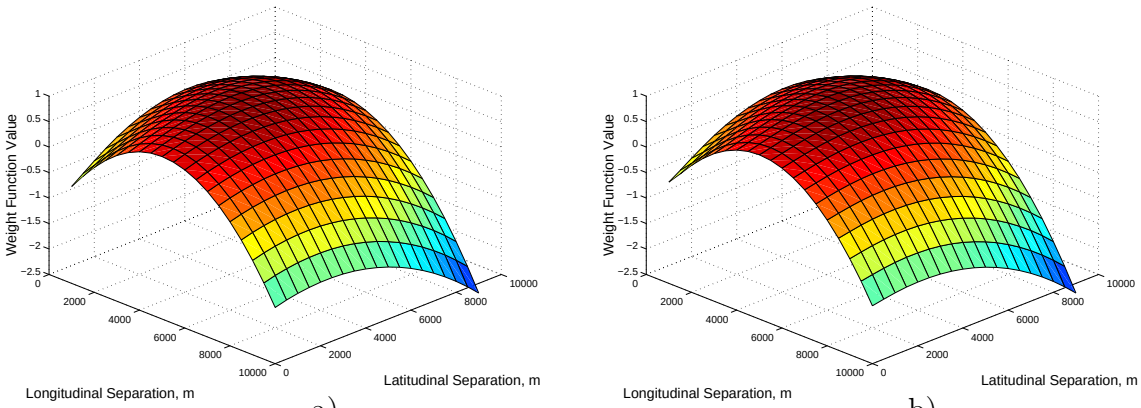

Figure 4.11: W_d for Two Values of Eccentricity: a) $e = 0$; b) $e = 0.00001$

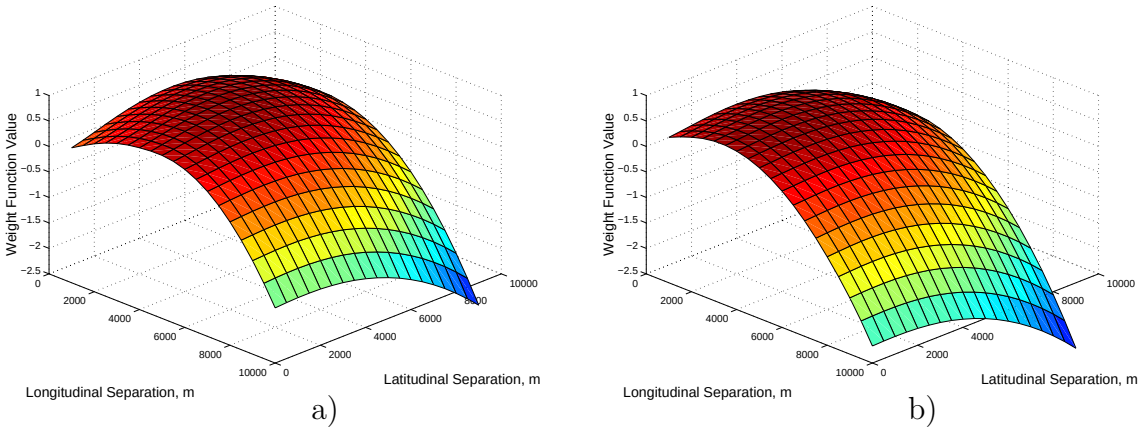

Figure 4.12: W_d for Two Values of Eccentricity: a) $e = 0.00005$; b) $e = 0.0001$

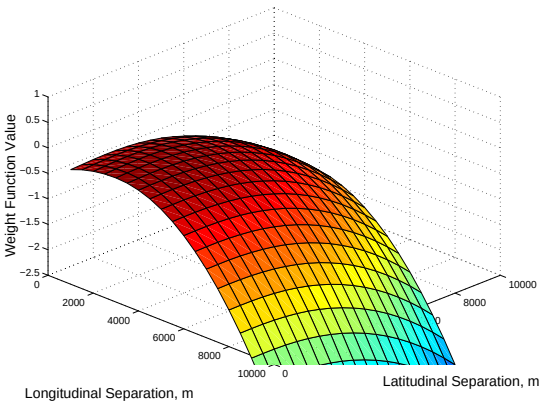

Figure 4.13: W_d for $e = 0.00015$

In sections 4.2–4.3 we apply the orbit performance measures based on angular and spatial separation to the diamond formation. We determine optimum configurations of the diamond formation for each measure. The effects of changing a and e on the orbit measures are also investigated. In the next section we investigate the application of the ISA measure to the diamond formation.

4.4 Weighted Separation Area Measure

The separation area measure integrates an instantaneous separation area metric, w_A, over an orbital period. The general form for W_A is

$$W_A = \frac{1}{T}\int_0^T w_A(A_s)\, dt \tag{4.20}$$

The function w_A is chosen to be consistent with the desired separation between spacecraft in formation. We have chosen a parabolic function of the form

$$w_A = (A_s - A_l)(A_s - A_u)/A_n \tag{4.21}$$

The upper limit on the separation area is defined as A_u, A_l is the lower limit on separation, and A_n is a normalization factor. We have chosen a characteristic value for A_l for a four spacecraft formation with separations on the order of 1000 m. This is consistent with the lower limits of w_α and w_d. Likewise, we have chosen a characteristic value for A_u for a four spacecraft formation with separations on the order of 5000 m. The normalization factor A_n ensures that the maximum value of $w_A = 1$.

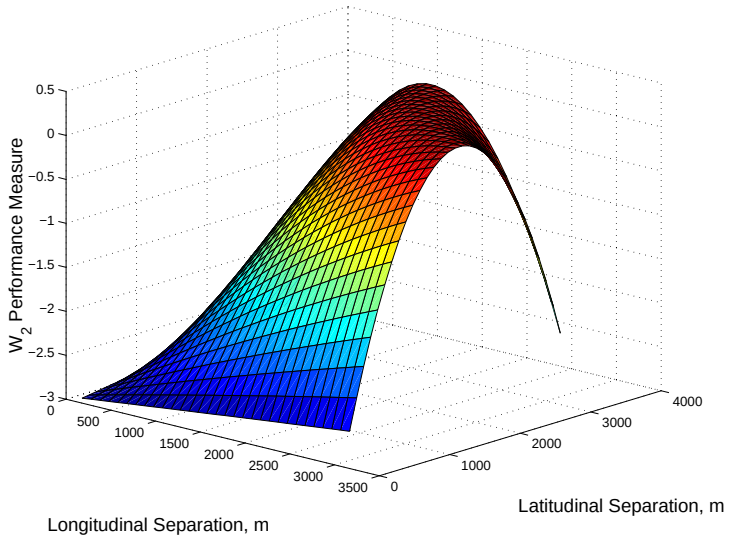

Figure 4.14: Weighted Separation Area Measure

The results of W_A applied to the diamond formation is seen in Fig. 4.14. The surface has a large region of near maximum weight as opposed to the surfaces in Figs. 4.2–4.3 that have distinct maxima. This demonstrates that there is a region within the design space that has similar separation area integrals over an orbit. For scenarios with large longitudinal and latitudinal separations the performance is poor because the separation area is not acceptable over most of the orbit. As d_{lon} and d_{lat} approach zero the separation area approaches zero and the performance measure tends toward the instantaneous value, $w_A(0) = -3$.

We wish to understand the effect of changing the semimajor axis on the separation area measure applied to the diamond formation. To determine the effect of changing semimajor axis on W_A we need to determine the quantity

$$\frac{\partial W_A}{\partial a} = \frac{1}{T}\int_0^T \frac{\partial w_A(A_s)}{\partial a} dt \tag{4.22}$$

The general form for the instantaneous area weight function is

$$w_A = c_1 A_s^2 + c_2 A_s + c_3 \tag{4.23}$$

The derivative on the right hand side of Eq. (4.22) can be written as

$$\frac{\partial w_A(A_s)}{\partial a} = 2c_1 A_s \frac{\partial A_s}{\partial a} + c_2 \frac{\partial A_s}{\partial a} \tag{4.24}$$

Hence the problem reduces to solving for the derivative $\partial A_s/\partial a$. The ISA is defined as the area on the sphere enclosed by the outermost subsatellite points. Because the relative position of the subsatellite points is not a function of the semimajor axis, A_s is also not a function a. Thus

$$\frac{\partial A_s}{\partial A} = 0 \qquad \Rightarrow \qquad \frac{\partial W_A}{\partial a} = 0 \tag{4.25}$$

and we see that W_A is independent of a.

In sections 4.2–4.4 we apply three orbit performance measures to the diamond formation. The diamond formation is defined by two variables, δ_{lon} and δ_{lat}. We now allow some of the orbits within the diamond formation more freedom. As a result, we can no longer determine optimum configurations using graphical techniques.

4.5 Higher Order Model

In section 4.1 we develop the diamond formation in terms of the variables δ_{lon} and δ_{lat}. According to this definition, the formation is defined by only two state variables. We now investigate a more general formation model using W_α with the parabolic instantaneous weight

function. Specifically, we allow Ω, i, and u for the two inclined orbits to vary. Hence our original definition of the latitudinal separation is no longer valid. The argument of latitude at epoch of the leading coplanar spacecraft is also allowed to vary. The resulting formation model has seven state variables. For seven state variables the solution can no longer be found using graphical techniques. Instead we use Newton's method to determine the solution. To initialize the algorithm we use the seven-state-space representation of the optimal two variable solution as an initial guess. The state vector is updated according to

$$\mathbf{x}_{i+1} = \mathbf{x}_i - \left[\frac{\partial \mathbf{W}_\alpha}{\partial \mathbf{x}}(\mathbf{x}_i)\right]^{-1} \mathbf{W}_\alpha(\mathbf{x}_i) \tag{4.26}$$

where i is the iteration number, $\mathbf{W}_\alpha(\mathbf{x}_i)$ is the gradient of W_α, and $\partial \mathbf{W}_\alpha(\mathbf{x}_i)/\partial \mathbf{x}$ is the Jacobian of W_α. Because analytical derivatives of W_α are not available, approximations for the gradient and the Jacobian are found using one-sided finite differencing as described in Stoer and Bulirsch *et al.*[19]

The optimum higher order solution has similar characteristics to the two-variable diamond formation previously discussed. However, the initial longitudinal position of the two spacecraft in the inclined orbits is shifted. To illustrate the results of the higher order solution, an exaggeration of the relative motion of the four spacecraft is plotted in Fig. 4.15. The latitudinal motion is unchanged. However, for clarity the longitudinal motion of the spacecraft in the inclined orbits is exaggerated. The inclined orbits produce figure-8 patterns in the relative reference frame. We label the left figure-8 as orbit 1 and the right as orbit 2. There is no relative motion between the coplanar spacecraft so they appear as fixed points. At the initial epoch the spacecraft in orbit 1 is at the top of the figure-8. We define clockwise

motion for a figure-8 to be the type of motion occurring in the upper half of the figure-8. A spacecraft in orbit 1 moves in clockwise motion according to this definition. A spacecraft in orbit 2 begins at the bottom of the figure-8 and also moves in clockwise motion. To scale, the actual motion of orbit 1 and orbit 2 appears as nearly straight vertical lines with a slight separation between them.

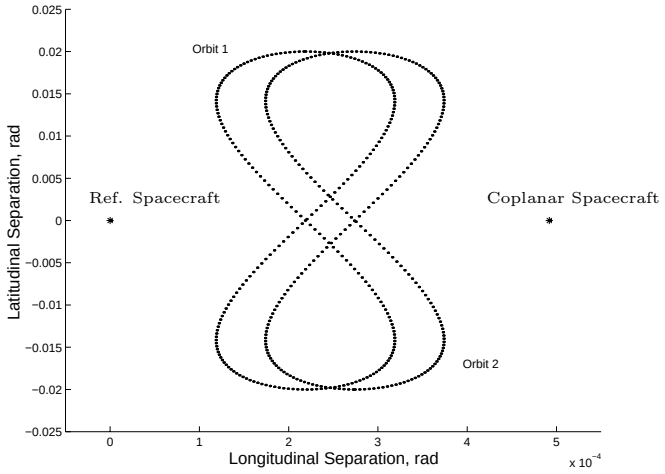

Figure 4.15: Exaggerated Relative Motion for Seventh-Order Solution

4.6 Summary

In general, due to orbit dynamics there is relative motion between spacecraft in formation over the course of an orbit. Therefore, the relative motion of spacecraft in formation must be appropriate to perform desired observations. In Ch. 3 we develop orbit performance measures based on the integration of an instantaneous metric over one orbit. The measures involve angular separation of spacecraft, the distance between spacecraft, and the ISA. In

this chapter we use the orbit model developed in Ch. 2 to develop a formation we call the diamond formation. Optimal configurations of the diamond formation are determined for each performance measure. We also investigate the effects of changing orbit parameters such as the semimajor axis, and eccentricity on the performance measures. The measures are shown to be independent of the semimajor axis. However, the effects of eccentricity are complex and dependent on the formation configuration. Finally, a more general formation model is considered and an optimal configuration is determined using Newton's Method.

Chapter 5

The Rotating Formation

The diamond formation has an opening and closing nature over an orbit as viewed from Earth. As a result, the relative positions of spacecraft in the formation are continually changing. A formation that maintains a constant shape over an orbit has several advantages over a dynamic array such as the diamond formation. The relative positions of spacecraft in a constant shape formation are nearly constant over an orbit. Therefore the formation can be designed such that the angular separations between spacecraft are near ideal for an entire orbit. A constant shape formation also avoids collisions between spacecraft. In this chapter we develop a constant shape formation we call the rotating formation. An algorithm is developed to place n satellites equally spaced in time around an ellipse in the relative reference frame. We apply the orbit measures to the rotating formation using the numerical techniques developed in Ch. 2. We also make some simplifying assumptions in order to develop analytical solutions for W_α.

5.1 Development of the Rotating Formation

We would like to develop a formation of n spacecraft so that the satellites move along an ellipse-like shape in a relative reference frame. A configuration of n spacecraft on an ellipse-like path is shown in Fig. 5.1. We measure the size of the ellipse using the angles δ_{lon} and δ_{lat}. The horizontal dimension of the ellipse is defined as δ_{lon} and the vertical dimension is defined as δ_{lat}. These definitions are consistent with the previous definitions for the diamond formation.

We need to generate a set of orbital elements for n spacecraft so that they move along the ellipse-like path with acceptable separations. We must first define the reference orbit and the relative reference frame $\mathcal{F}_{rel}$. We choose the reference orbit to be circular and equatorial with a true longitude at epoch of ℓ_{ref}. The origin of $\mathcal{F}_{rel}$ is attached to a reference spacecraft that

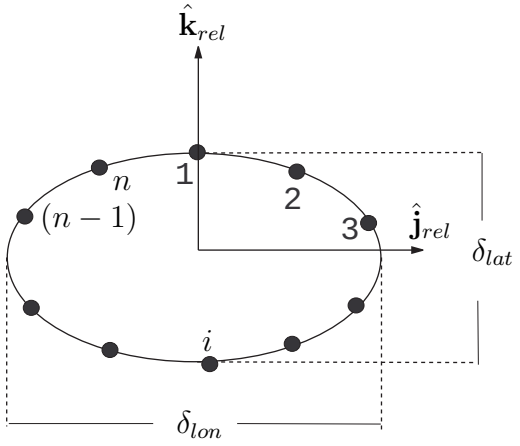

Figure 5.1: Geometry of the Rotating Formation

moves along the reference orbit. The x_{rel}-axis is in the direction of the reference spacecraft's position vector. The y_{rel}-axis lies along the reference spacecraft's velocity vector direction.

By this definition the y_{rel}-axis is always tangent to the reference orbit. The z_{rel}-axis is chosen to complete the right-handed set, and is in the orbit normal direction.

We need to determine the dimensions of the relative orbit in terms of the orbital elements of the spacecraft in formation. We limit our discussion to orbits that are nearly circular and result in small displacements from the reference orbit. In doing so we require that the spacecraft motion occurs in nearly the same plane as the reference motion. Therefore, the along-track displacements in the relative motion are primarily due to the eccentricity of the orbits. With these assumptions we can determine the dependence of δ_{lon} and δ_{lat} on the orbital elements.

We see in Fig. 5.2 a view of the ellipse-like path of the rotating formation shown in $\mathcal{F}_R$. The vector $\mathbf{r}_1$ describes the position of an arbitrary spacecraft. The true anomaly, ν, for the spacecraft is measured from the $\hat{\mathbf{i}}_1$ axis. The quantity y_{lon} is the along-track component of angular separation of the spacecraft in $\mathcal{F}_{rel}$. Therefore, y_{lon} is defined as an angle and not a distance. From inspection of Fig. 5.2 we see that the angle δ_{lat} is due to the difference in inclination between the orbit and the reference orbit. The expression for δ_{lat} in terms of the inclination is simply

$$\delta_{lat} = 2i \tag{5.1}$$

Recall that we assume the out of plane motion does not affect the along-track angular separation. Therefore we can determine δ_{lon} by investigating the projection of the motion in

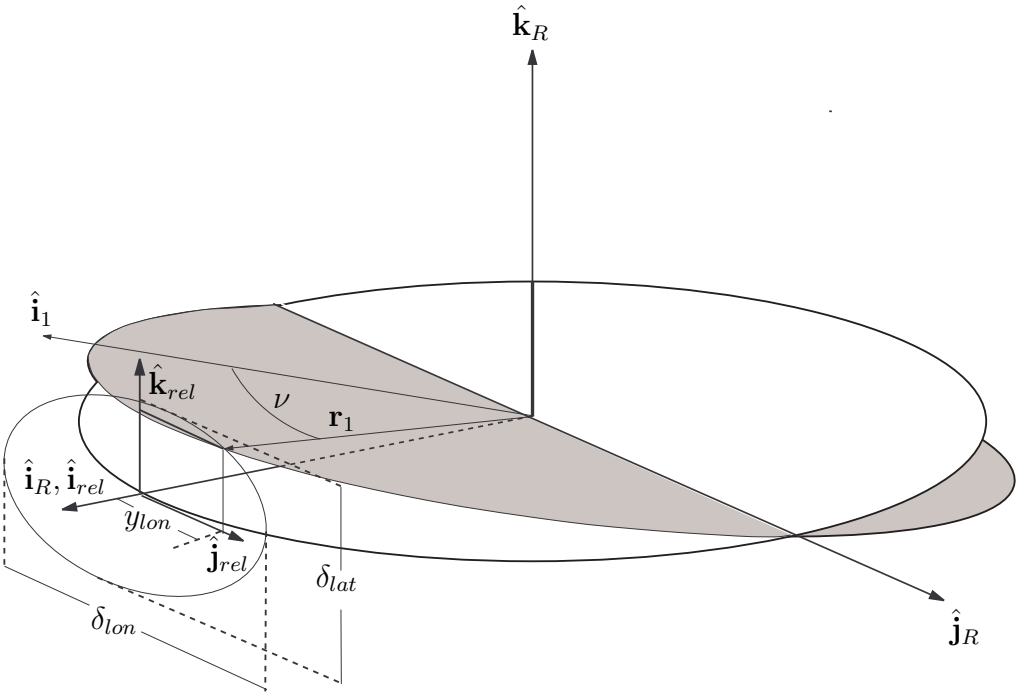

Figure 5.2: The Rotating Formation Seen in $\mathcal{F}_R$ and $\mathcal{F}_{rel}$

the $x_R - y_R$ plane as seen in Fig. 5.3. To determine δ_{lon} we must first develop an expression for y_{lon}. From inspection of Fig. 5.3 we can write

$$y_{lon} = \nu - \theta \tag{5.2}$$

where θ is the angle between $\hat{\mathbf{i}}_{rel}$ and $\hat{\mathbf{i}}_1$. We can express θ as

$$\theta = M_{0_{rel}} + \eta t \tag{5.3}$$

where $M_{0_{rel}}$ is the angle between $\hat{\mathbf{i}}_{rel}$ and $\hat{\mathbf{i}}_1$ at the initial epoch. The horizontal dimension, δ_{lon}, is simply twice the maximum in the along-track separation:

$$\delta_{lon} = 2y_{lon}|_{max} \tag{5.4}$$

For small e we can write

$$\nu = M_{0_1} + \eta t + 2e \sin\left(M_{0_1} + \eta t\right) \tag{5.5}$$

as found in Vallado,[20] where M_{0_1} is the mean anomaly of $\mathbf{r}_1$ at the initial epoch. Substituting Eqs. (5.3) and (5.5) into Eq. (5.2) we obtain

$$y_{lon} = 2e \sin\left(M_{0_1} + \eta t\right) + M_{0_1} - M_{0_{rel}} \tag{5.6}$$

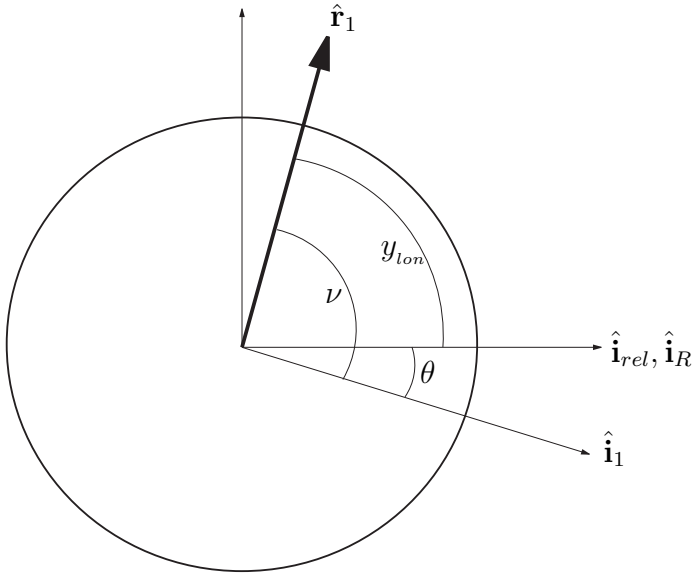

Figure 5.3: The Rotating Formation Projected into the $x_R - y_R$ Plane

Recall that M_{0_1} and $M_{0_{rel}}$ are constants so

$$y_{lon}|_{max} = 2e \tag{5.7}$$

Substituting Eq. (5.7) into Eq. (5.4)we obtain

$$\delta_{lon} = 4e \tag{5.8}$$

A similar result was arrived at by Chichka[15] using a second-order approximation.

We now know the dimensions of the rotating formation in terms of e and i. However, we need to develop an algorithm to place n spacecraft in an ellipse-like formation defined by δ_{lon} and δ_{lat}.

5.2 Spacecraft Placement in the Rotating Formation

Knowing δ_{lon} and δ_{lat} we wish to develop an algorithm to place n spacecraft along the ellipse-like path in the relative reference frame. The spacecraft can be placed in the formation in three different configurations: equal angle separations, equal arc length separations, and equal time separations. We develop an algorithm to place the spacecraft around the ellipse-like path with equal time separations. For circular formations, equal time separation is equivalent to equal arc length and equal angle separation. For ellipse-like formations the relationship between the three configurations is non-trivial. We develop the formation by first investigating the requirements to place a single spacecraft on an ellipse-like path defined by δ_{lon} and δ_{lat}. Then we generalize the method to include n spacecraft spaced equally in time.

To develop the algorithm we must consider two reference frames: the relative reference frame $\mathcal{F}_{rel}$ previously discussed, and an inertial reference frame $\mathcal{F}_R$. A diagram showing $\mathcal{F}_R$ and the configuration of the relative reference frame at two different epochs is shown in Fig. 5.4. Frame $\mathcal{F}_R$ is not equivalent to the Earth-centered inertial frame $\mathcal{F}_I$ commonly

found in the literature. The frame $\mathcal{F}_R$ is fixed in inertial space with its origin at the center of the Earth. However, its axes can be defined by any arbitrary right-handed system. The result is that the x_R-y_R plane of $\mathcal{F}_R$ is not the Earth's equatorial plane, it is the orbital plane of the reference circular orbit. The orbital elements used to describe the rotating formation are used according to their classical definition described in Ch. 2, but for generality they are measured with respect to $\mathcal{F}_R$ unless otherwise stated.

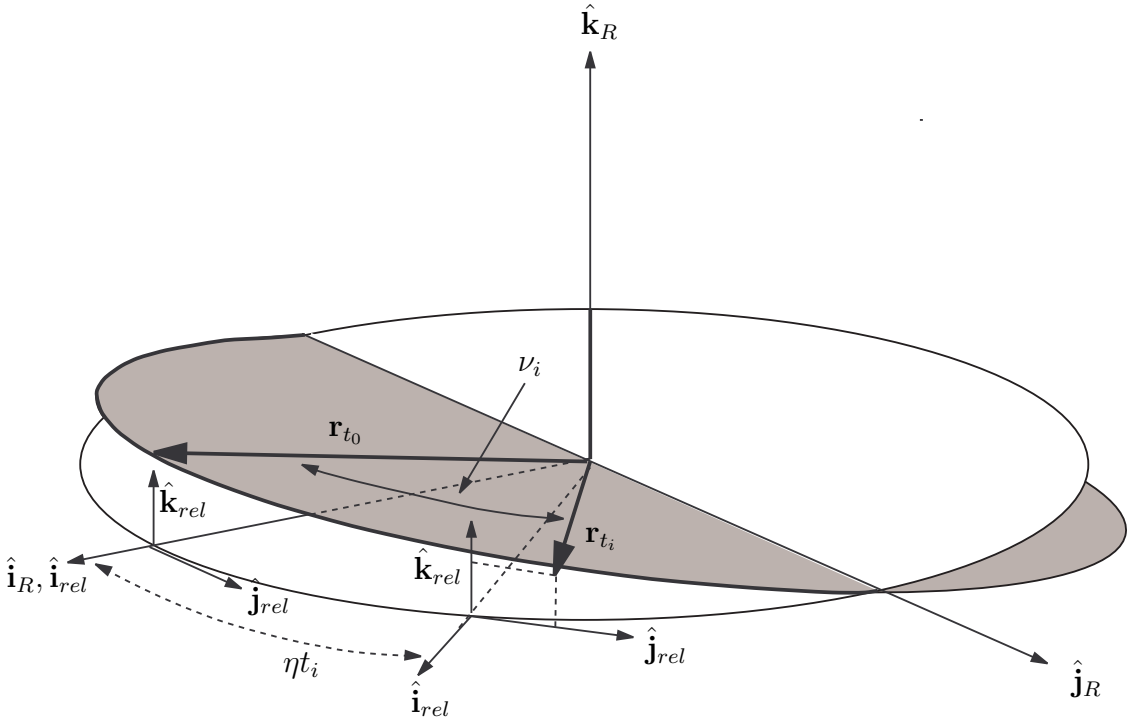

Figure 5.4: Time Evolution of the Rotating Formation

We know from Eqs. (5.1) and (5.8) that the dimensions of the relative motion path in $\mathcal{F}_{rel}$ depends only on e and i. Therefore, for all the spacecraft to move along an ellipse of the same dimensions in $\mathcal{F}_{rel}$, all the orbits in the formation must have a common e and i.

Solving for i in Eq. (5.1) yields

$$i = \delta_{lat}/2 \tag{5.9}$$

From Eq. (5.8) the eccentricity can be written as

$$e = \delta_{lon}/4 \tag{5.10}$$

To ensure a cohesive formation, all the orbits must also have the same semimajor axis. Therefore, only ω, Ω, and ν may vary for the orbits in the rotating formation.

At the initial epoch we choose the origin of the reference orbital frame to lie along the x_R-axis in a circular orbit whose plane of motion is the $x_R - y_R$ plane. Hence the orbital elements of the reference orbit are

$$a_{ref} = a \quad e_{ref} = 0 \quad i_{ref} = 0 \quad \ell_{ref} = 0 \tag{5.11}$$

We begin constructing the formation by placing a spacecraft in position 1 shown in Fig. 5.1. We choose the relative motion to be clockwise. For clockwise motion to occur the spacecraft at position 1 must be moving in the y_{rel} direction faster than the origin of the reference orbit. Therefore, we place spacecraft 1 at the periapsis of its orbit:

$$\nu_1 = 0 \tag{5.12}$$

We must choose ω_1 and Ω_1 to position the periapsis of orbit 1 over $\hat{\mathbf{i}}_R$. By inspection of Fig. 5.4 we see that this is accomplished by choosing

$$\Omega_1 = 3\pi/2 \qquad \omega_1 = \pi/2 \tag{5.13}$$

In summary, the orbital elements to position a spacecraft at position 1 in $\mathcal{F}_{rel}$ with the reference orbit defined by Eq. (5.11) are

$$a_1 = a \quad e_1 = \delta_{lon}/4 \quad i_1 = \delta_{lat}/2 \quad \omega_1 = \pi/2 \quad \Omega_1 = 3\pi/2 \quad \nu_1 = 0 \tag{5.14}$$

We now develop an algorithm to place n satellites spaced equally in time along the ellipse-like path seen in Fig. 5.1. For all satellites to move along the same path in $\mathcal{F}_R$ we require that all the orbits share a common a, e, and i. However, we must determine ω, Ω, and ν for the remaining orbits. Recall that the orbital period T is given by

$$T = 2\pi\sqrt{\frac{a^3}{\mu}} \tag{5.15}$$

The time of separation, t_s, between spacecraft in an equal time formation is given by

$$t_s = T/n = \frac{2\pi}{n}\sqrt{\frac{a^3}{\mu}} \tag{5.16}$$

To determine the orbital elements of the i^{th} spacecraft in formation we propagate orbit 1 through time t_i where

$$t_i = (i-1)t_s \tag{5.17}$$

The configuration of spacecraft 1 and the reference orbit at the initial epoch, t_1, and at t_2 can be seen in Fig. 5.4. We need to determine ν_{t_i}, the value of ν for orbit 1 after the passage of time t_i. Recall that for small e we can write

$$\nu_{t_i} = M_{t_i} + 2e\sin M_{t_i} \tag{5.18}$$

where

$$M_{t_i} = M_0 + (i-1)\eta t_s \tag{5.19}$$

Recall that the true anomaly for orbit 1 at the initial epoch is zero. Therefore, we know that $M_0 = 0$. Now we can write

$$\nu_{t_i} = (i-1)\eta t_s + 2e\sin\left((i-1)\eta t_s\right) \tag{5.20}$$

Substituting Eq. (5.16) into Eq. (5.20) we obtain

$$\nu_{t_i} = \frac{2\pi}{n}(i-1) + 2e\sin\left(\frac{2\pi}{n}(i-1)\right) \tag{5.21}$$

For a Keplerian orbit only ν changes with time. Therefore we now know the orbital elements to space n spacecraft equally in time in $\mathcal{F}_R$ from Eq. (5.21). However, we need to determine the elements to space n spacecraft equally in time in $\mathcal{F}_{rel}$. We need to determine the new configuration of $\mathcal{F}_{rel}$ after the passage of time t_i. Then we can determine the orbital elements to space n spacecraft equally in time in $\mathcal{F}_{rel}$ by a coordinate transformation.

The frame $\mathcal{F}_{rel}$ is defined by a circular, equatorial reference orbit in $\mathcal{F}_R$. Therefore the motion of the coordinate system $\mathcal{F}_{rel}$ after time t_i is simply a 3-rotation through the angle $\theta = \eta t_i$. Performing a 3-rotation through ηt_i to $\mathcal{F}_{rel}$ is equivalent to rotating Ω_i through an angle $\theta = -\eta t_i$. Therefore to have n spacecraft spaced equally in time in $\mathcal{F}_{rel}$ we write

$$\Omega_i = 3\pi/2 - \eta t_i = \frac{3\pi}{2} - \frac{2\pi(i-1)}{n} \tag{5.22}$$

In summary, to obtain the orbital elements to place the i^{th} spacecraft in an equal time formation in $\mathcal{F}_{rel}$ we propagate orbit 1 through ν_i as defined in Eq. (5.21). Then we rotate the longitude of the ascending node backwards to Ω_i as defined by Eq. (5.22) to account for the motion of $\mathcal{F}_{rel}$. Hence a, e, i, and ω are the same for all orbits in the formation. The

true anomaly and the longitude of ascending node are given by Eqs. (5.21) and (5.22). In general, the i^{th} set of orbital elements is given by

$$\begin{gathered} a_i = a \quad e_i = \delta_{lon}/4 \quad i_i = \delta_{lat}/2 \quad \omega_i = \pi/2 \quad \Omega_i = 3\pi/2 - \tfrac{2\pi(i-1)}{n} \\ \nu_i = \tfrac{2\pi}{n}(i-1) + 2e\sin\left(\tfrac{2\pi}{n}(i-1)\right) \end{gathered} \tag{5.23}$$

where $1 \leq i \leq n$. We now investigate the application of the orbit performance measures to the rotating formation.

5.3 Application of the Orbit Measures to the Rotating Formation

In sections 5.3.1–5.3.3 we investigate the application of the orbit performance measures to the rotating formation. We apply the measures to a formation of four spacecraft using numerical techniques in sections 5.3.1–5.3.2. In section 5.3.3 we develop an analytic solution for W_α and determine optimum configurations for different n.

5.3.1 Angular Measure

Application of W_α to the rotating formation with $n = 4$ using the quartic and parabolic weight functions is seen in Fig. 5.5. The results for the quartic weight are seen on the left. The parabolic results are shown on the right. Both weight functions find the optimum to occur for $d_{lon} = 3500$ m and $d_{lat} = 3500$ m. If initial conditions are poor the formation

will perform poorly over the entire orbit because the rotating formation maintains a nearly constant shape over an orbit. For this reason both formations perform poorly when $d_{lon} \approx 0$ and $d_{lat} \approx 0$, which is consistent with results for the diamond formation. Similarly, scenarios with $d_{lon} > 5000$ m and $d_{lat} > 5000$ m result in low performance because the maximum upper limit on separation according to both the parabolic and quartic weights occurs at an angle that results in separations of 5000 m at a radius of 8000 km.

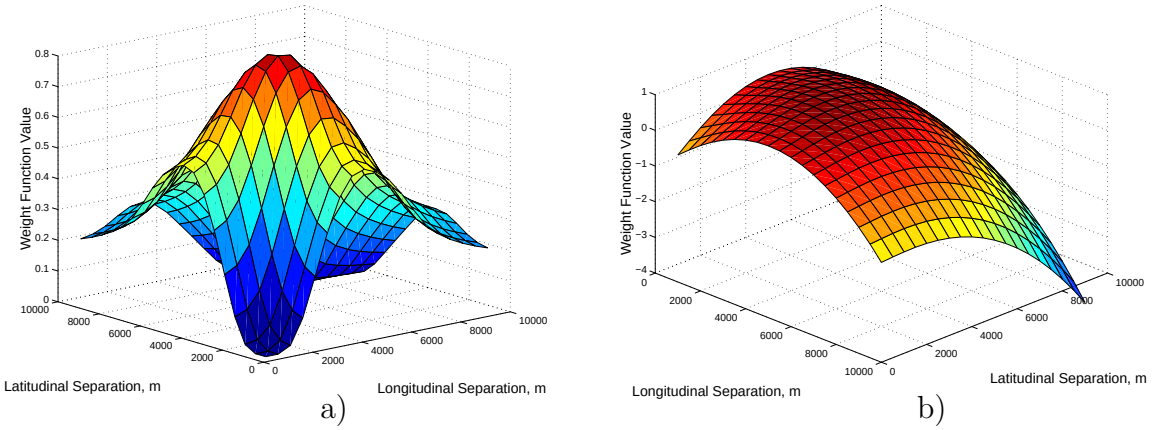

Figure 5.5: W_α for the Rotating Formation: a) Quartic ; b) Parabolic

We wish to determine the effect of changes in semimajor axis and eccentricity on W_α as applied to the rotating formation. In section 4.2.2 we show that W_α is not dependent on a for any formation, because $\alpha \neq f(a)$. However, the effects of eccentricity are unique to each formation. Recalling Eq. (5.8) we know that $\delta_{lon} = 4e$ for small e. Hence when we examine the variation of W_α with δ_{lon} we obtain information about the change in W_α with changes in eccentricity.

Figure 5.6 shows the weight function plotted as a function of eccentricity and d_{lat}. Performance is poor for eccentricities less than 5×10^{-4} because eccentricities near zero result

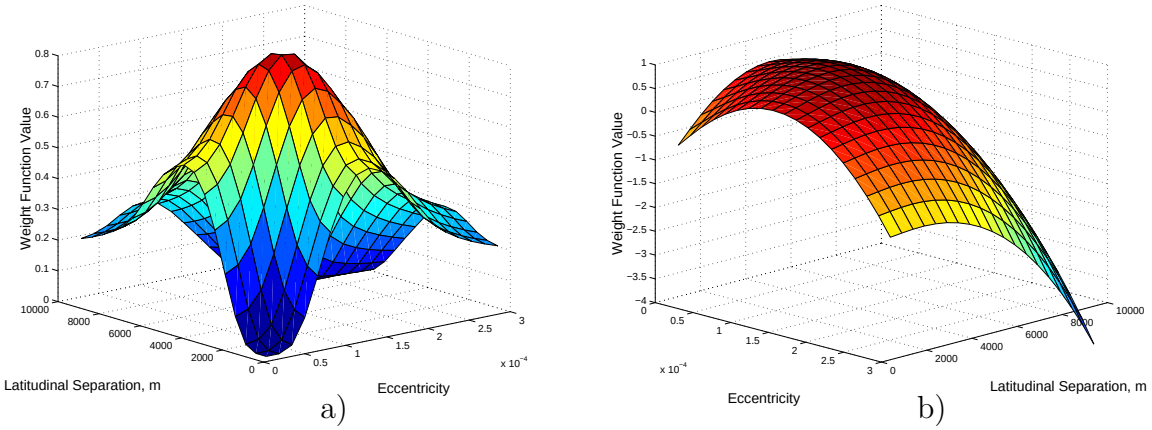

Figure 5.6: W_α *vs.* e for the Rotating Formation: a) Quartic ; b) Parabolic

in longitudinal separations near zero which is poor according to both w_p and w_q. As eccentricity increases from zero the performance improves up to a maximum that occurs near the eccentricity required to provide a d_{lon} of 3000 m. This is because the maximum in w_α is chosen to occur at an angle producing a spatial separation of 3000 m at a semimajor axis of 8000 km. A further increase in the eccentricity results in a decrease in performance because the dimension of d_{lon} is unacceptable according to the instantaneous weight.

5.3.2 Distance Measure

We now apply the distance measure W_d to the rotating formation with $n = 4$. Figure 5.7 shows the results for two different semimajor axes of $a = 8000$ km and $a = 10000$ km. According to W_d the optimum in performance occurs at a d_{lon} of 3500 m and a d_{lat} of 3000 m for both values of a. This value is close to the maximum obtained using W_α which occurred for $d_{lon} = 3500$ m and $d_{lat} = 3500$ m. The performance is poor when d_{lon} and d_{lat} are less than 1000 m which is consistent with the definition of w_d. The performance is also

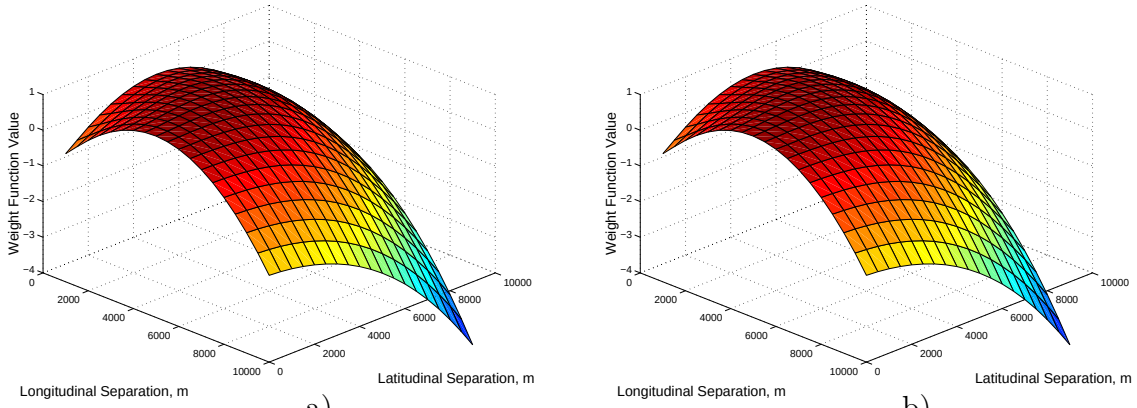

Figure 5.7: W_d Applied to the Rotating Formation: a) a=8000 km ; b) a=10000 km

poor for values of d_{lon} and d_{lat} greater than 5000 m.

In Fig. 5.7 W_d for two different values of semimajor axis is found. On the left the measure is shown for $a = 8000$ km. On the right the results for $a = 10000$ km are shown. In Ch. 4 we show that the distance measure is not a function of the semimajor axis if the orbits have small eccentricities. This result is confirmed by comparing the two plots created using different values of a.

5.3.3 An Analytic Solution

In general W_α does not permit a closed-form analytic solution. However, we can make some simplifying assumptions and apply the metric to the rotating formation to obtain an analytic solution. We wish to find a closed-form solution to

$$W_\alpha = \frac{1}{\eta_s T} \int_0^T \sum_{i=1}^{n-1} \sum_{j=i+1}^{n} w_\alpha(\alpha_{ij})\, dt \tag{5.24}$$

where

$$w_\alpha(\alpha_{ij}) = c_1\alpha_{ij}^2 + c_2\alpha_{ij} + c_3 \tag{5.25}$$

In Ch. 4 we assume an instantaneous function of the form

$$w_\alpha(\alpha_{ij}) = \frac{1}{\alpha_s}(\alpha_{ij} - \alpha_u)(\alpha_{ij} - \alpha_l) \tag{5.26}$$

where α_u and α_l are the upper and lower limits on angular separation respectively and α_s is a normalization factor. However, the analytic solution for W_α is simpler when solved using the equivalent form seen in Eq. (5.25). We substitute the relations

$$c_1 = 1/\alpha_s \tag{5.27}$$

$$c_2 = -(\alpha_u + \alpha_l)/\alpha_s \tag{5.28}$$

$$c_3 = \alpha_u\alpha_l/\alpha_s \tag{5.29}$$

at the end of the analysis to obtain a solution in terms of α_l, α_u, and α_s.

Recall that a rotating formation composed of n spacecraft can be completely defined by the four variables a, n, e, and i. Therefore, we need to determine an expression for α_{ij} in terms of these four variables. A solution for α_{ij} in terms of a, n, e, and i allows a solution for W_α of the form

$$W_\alpha = f(n, a, e, i, c_1, c_2, c_3) \tag{5.30}$$

We use the cross product to obtain an expression for α_{ij}:

$$\| \mathbf{r}_i \times \mathbf{r}_j \| = r_i r_j \sin\alpha_{ij} \tag{5.31}$$

For close formations α_{ij} is small so we can assume

$$\sin \alpha_{ij} \approx \alpha_{ij} \tag{5.32}$$

Solving for α_{ij} we obtain the expression

$$\alpha_{ij} = \frac{\| \mathbf{r}_i \times \mathbf{r}_j \|}{r_i r_j} \tag{5.33}$$

We can write the vectors $\mathbf{r}_i$ and $\mathbf{r}_j$ in their own perifocal systems as

$$\mathbf{r}_{i_p} = \frac{a(1-e^2)}{1+e\cos\nu_i} \begin{bmatrix} \cos\nu_i & \sin\nu_i & 0 \end{bmatrix}^T \tag{5.34}$$

and

$$\mathbf{r}_{j_p} = \frac{a(1-e^2)}{1+e\cos\nu_j} \begin{bmatrix} \cos\nu_j & \sin\nu_j & 0 \end{bmatrix}^T \tag{5.35}$$

where ν_i and ν_j are given by Eq. (5.23).

To use Eq. (5.33) we must rotate the vectors into the inertial frame using the appropriate rotation matrix. We can construct the rotation matrix for the i^{th} position vector using

$$\mathbf{R}_i^{Ip} = \mathbf{R}_3(-\Omega_i)\mathbf{R}_1(-i)\mathbf{R}_3(-\omega) \tag{5.36}$$

where Ω_i is given in the orbital element set in Eq. (5.23). Then we can write the inertial representations of $\mathbf{r}_i$ and $\mathbf{r}_j$ using

$$\mathbf{r}_{i_I} = \mathbf{R}_i^{Ip}\mathbf{r}_{i_p} \tag{5.37}$$

$$\mathbf{r}_{j_I} = \mathbf{R}_j^{Ip}\mathbf{r}_{j_p} \tag{5.38}$$

We now have the information required to evaluate α_{ij} from Eq. (5.33). The expression, which is not shown here, is a non-trivial transcendental function of the form

$$\alpha_{ij} = f(n, a, e, i) \tag{5.39}$$

In general, solving W_α requires integrating the motion over an orbit. However, for special configurations of the rotating formation, the relative spacing between the spacecraft is nearly constant over an orbit. This is true for near circular rotating formations when

$$\delta_{lon} \approx \delta_{lat} \tag{5.40}$$

The relative positions are also nearly constant over an orbit for formations composed of a large number of spacecraft. In Fig. 5.8 we see a rotating formation of four spacecraft. The shaded circles represent the positions of four spacecraft at the initial epoch. The white circles represent the positions of the spacecraft after a small passage of time, Δt . The relative positions, and hence the angular separations, have changed after the time Δt. However,

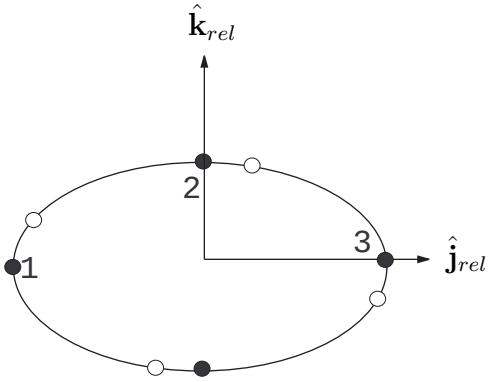

Figure 5.8: Rotating Formation of Four Spacecraft

when the spacecraft at position 1 reaches position 2 the relative positions of the spacecraft will be nearly the same as at the initial epoch. The relative positions are not exactly the same because all of the spacecraft in formation are at different points in an elliptical orbit. For example, for this configuration spacecraft 2 is at periapsis and spacecraft 1 is at a true anomaly given by Eq. (5.23) with $i = 4$. Therefore the time for spacecraft 1 to reach position

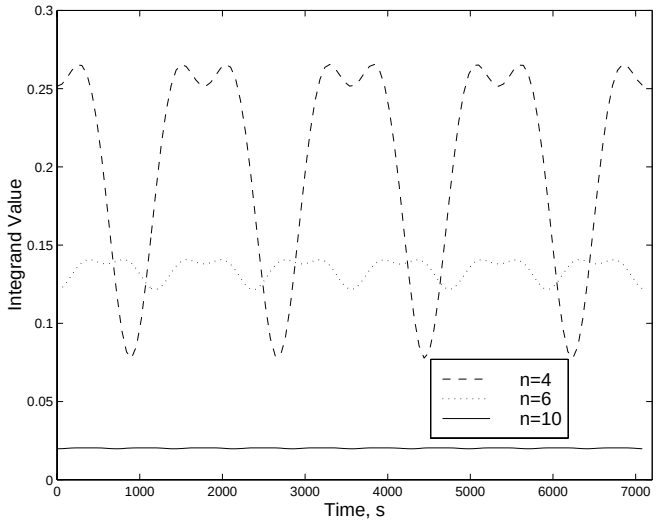

Figure 5.9: Integrand *vs.* Time for a Highly Elliptical Formation

2 is slightly different from the amount of time for spacecraft 2 to reach position 3. For a four-spacecraft formation the relative positions are nearly the same after a passage of time $T/4$. In general, for a formation of n spacecraft, the relative positions are nearly equivalent after time T/n. Therefore the period of the formation decreases with n. More importantly though, as n increases the amplitude of the integrand in Eq. (5.24) goes to zero. This is demonstrated in Fig. 5.9. We see a plot of the integrand over an orbit period for $n = 4, 6, 10$. The plot was created for a highly elliptical formation with $d_{lon} = 6000$ m and $d_{lat} = 1000$ m. As n increases we see that the period and amplitude of the motion decrease. Hence, the relative positions of the spacecraft are nearly constant for large n.

If the relative motion of a formation is nearly constant over an orbit we can neglect the integral in

$$W_\alpha = \frac{1}{\eta_s T} \int_0^T \sum_{i=1}^{n-1} \sum_{j=i+1}^{n} w(\alpha_{ij})\, dt \tag{5.41}$$

and express W_α as $\tilde{W}_\alpha$ where

$$\tilde{W}_\alpha = \frac{1}{\eta_s} \sum_{i=1}^{n-1} \sum_{j=n+1}^{n} w(\alpha_{ij}) \tag{5.42}$$

With Eqs. (5.42), (5.33), and (5.25) we have the tools to express W_α analytically. We are interested in the dimensions of the rotating formation that result in optimum performance. Recall that the shape of the rotating formation is determined by e and i. The analytic expression of W_α is a non-trivial function in terms of seven variables. We need to simplify the expression to solve for optimum configurations in terms of e and i. As shown in Ch. 4, W_α is not dependent on a. At this point in the analysis the expression for W_α is extremely complicated and it is a non-trivial task to simplify it to a form where a does not appear. However, we see that W_α is indeed independent of a as further assumptions and simplifications are made.

To obtain an expression for W_α we need to evaluate the summation in Eq. (5.42) for a given n. We choose $n = 4$ to demonstrate the techniques used to obtain the optimum. We then present results for several values of n to determine trends in the optimum solutions for changing n.

We now have W_α in terms of e, i, c_1, c_2, and c_3. We can expand the expression to third-order in small e and i about $e = 0$ and $i = 0$ to obtain an approximate expression. However, the resulting expression has a singularity at $e = 0$. Plotting the exact expression for W_α in negative i and e, as shown in Fig. 5.10, lends some understanding. We see there is a cusp at $e = 0$ and $i = 0$. Therefore the derivative is undefined at this point. We need to

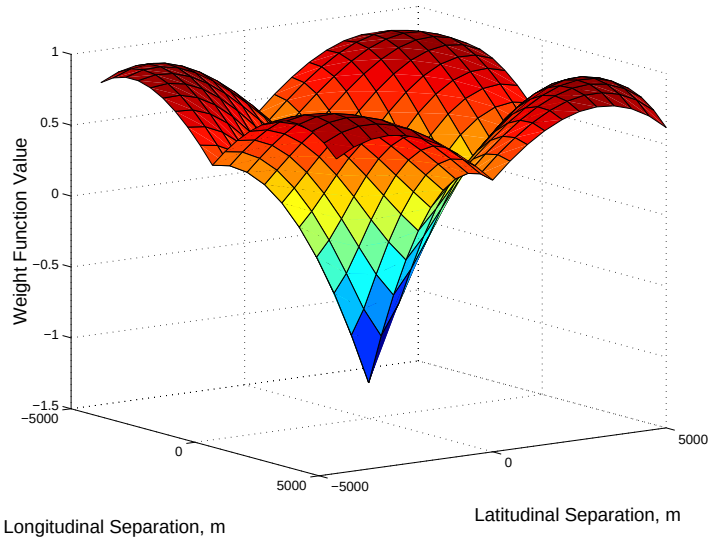

Figure 5.10: The Singularity in Eccentricity

expand about another point where there is no singularity. To do so we make a substitution using

$$e = \frac{i}{2}(1+\epsilon) \tag{5.43}$$

where $0 < \epsilon \ll 1$ is a small dimensionless parameter. This substitution eliminates the singularity in e. Expanding the resulting expression to third-order in i and ϵ yields an approximate expression for W_α:

$$W_a = -\frac{11c_2i^3}{18} - \frac{13c_2i^3}{18\sqrt{2}} + \frac{8c_1i^2\epsilon}{3} + \frac{8c_1i^2}{3} + \frac{c_2\epsilon^2 i}{6\sqrt{2}} + \frac{\sqrt{2}c_2\epsilon i}{3} + \frac{c_2\epsilon i}{3} + \frac{2\sqrt{2}c_3 i}{3} + \frac{2c_2 i}{3} + c_3 \tag{5.44}$$

To solve for the e and i resulting in an optimum we must solve the set of simultaneous equations

$$\frac{\partial W_a}{\partial i} = 0 \tag{5.45}$$

$$\frac{\partial W_a}{\partial e} = 0 \tag{5.46}$$

for e and i. However, we first must find expressions for the derivatives $\partial W_a/\partial i$ and $\partial W_a/\partial e$ in terms of e. Taking the first derivative of Eq. (5.44) with respect to i yields

$$\frac{\partial W_a}{\partial i} = \frac{64c_1(1+\epsilon)i + c_2(8(1+\sqrt{2}) + 4(1+\sqrt{2})\epsilon + \sqrt{2}\epsilon^2 - (22+13\sqrt{2})i^2}{12} \tag{5.47}$$

To obtain an expression in terms of e we substitute using

$$\epsilon = 2\frac{e}{i} - 1 \tag{5.48}$$

to obtain

$$\frac{\partial W_a}{\partial i} = \frac{128c_1ei^2 + c_2(4\sqrt{2}e^2 + 4(2+\sqrt{2})ei + i^2(4+5\sqrt{2} - (22+13\sqrt{2})i^2))}{12i^2} \tag{5.49}$$

Taking the partial derivative of W_a with respect to ϵ yields

$$\frac{\partial W_a}{\partial \epsilon} = \frac{i^2\left(c_2(2+2\sqrt{2}+\sqrt{2}\epsilon) + 16c_1i\right)}{12} \tag{5.50}$$

To determine an expression in terms of e we multiply by $\partial\epsilon/\partial e$ where

$$\frac{\partial \epsilon}{\partial e} = 2/i \tag{5.51}$$

The derivative with respect to e is

$$\frac{\partial W_a}{\partial e} = \frac{\partial W_a}{\partial \epsilon}\frac{\partial \epsilon}{\partial e} = \frac{i\left(16c_1i^2 + c_2\left(2\sqrt{2}e + (2+\sqrt{2})i\right)\right)}{12} \tag{5.52}$$

Solving Eqs. (5.49) and (5.52) simultaneously for e and i we obtain expressions for e and i that yield an optimum in W_α. The expressions are complex and not shown here. However, there is a relation between the optimum e and i such that

$$e_{opt} = i_{opt}/2 \tag{5.53}$$

Recall that we assume $n = 4$ in order to obtain an explicit expression for W_α. Therefore Eq. (5.53) appears to be dependent on the assumption that we have a four spacecraft formation. However, if we assume $n = 2, 3, 5, 6, 10$ we obtain the same result.

We now investigate the physical implications of Eq. (5.53). Recall that

$$\delta_{lon} = e/4 \tag{5.54}$$

$$\delta_{lat} = i/2 \tag{5.55}$$

We can rewrite these expressions as

$$e = \delta_{lon}/4 \tag{5.56}$$

$$i = \delta_{lat}/2 \tag{5.57}$$

Substituting Eqs. (5.56–5.57) into Eq. (5.53) we see that

$$\delta_{lon} = \delta_{lat} \tag{5.58}$$

Hence the ideal rotating formation according to W_α is circular.

For a circular formation we can make an additional simplification by writing

$$e = i/2 \tag{5.59}$$

We now substitute Eq. (5.59) into Eq. (5.42) to obtain an expression for $\tilde{W}_\alpha$ in terms of i, c_1, c_2, and c_3. Recall that the only assumptions made to arrive at Eq. (5.42) are small angles and that the integrand in Eq. (5.41) is constant in time. Therefore we need to simplify $\tilde{W}_\alpha$ by expanding in a power series to second-order in i.

We investigate a larger formation with $n = 8$. A second order expansion in i for $n = 8$ yields

$$W_a = \frac{16c_1}{7} i^2 + c_2 \left(\frac{4}{7\sqrt{2-\sqrt{2}}} + \frac{2\sqrt{2}}{7} + \frac{2}{7} \right) i + c_3 \tag{5.60}$$

To solve for the maximum we must solve $\partial W_a / \partial i = 0$ for the inclination.

$$\frac{\partial W_a}{\partial r} = \frac{32c_1}{7} i + \left(\frac{2(1+\sqrt{2})}{7} + \frac{4}{7\sqrt{2-\sqrt{2}}} \right) c_2 \tag{5.61}$$

For circular formations the radius of the formation is simply the inclination of the orbits composing the formation. Therefore, solving for the optimum radius, r_o, and substituting for c_1, c_2, and c_3 using Eqs. (5.27–5.29) we obtain

$$r_o = \left(\frac{1}{16} + \frac{\sqrt{2}}{16} + \frac{1}{16} \left(\sqrt{2-\sqrt{2}} + \sqrt{2+\sqrt{2}} \right) \right) (\alpha_l + \alpha_u) \tag{5.62}$$

We define a new angle, α_m, such that

$$\alpha_m = \frac{\alpha_u + \alpha_l}{2} \tag{5.63}$$

This angle is the ideal separation angle according to the instantaneous weight function w_q. We can rewrite r_o in terms of α_m:

$$r_o = \left(\frac{1}{8} + \frac{\sqrt{2}}{8} + \frac{1}{8} \left(\sqrt{2-\sqrt{2}} + \sqrt{2+\sqrt{2}} \right) \right) \alpha_m \tag{5.64}$$

We can apply the same techniques to find the optimum radius for different values of n. The results for different values of n are

$$n = 2 \quad r_o = \frac{1}{2} \alpha_m \tag{5.65}$$

$$n = 3 \quad r_o = \left(-8\sqrt{3}\alpha_m \right) / \left(-24 + \sqrt{3}\alpha_m \right) \tag{5.66}$$

$$n = 4 \quad r_o = \frac{1}{4}\left(1+\sqrt{2}\right)\alpha_m \tag{5.67}$$

$$n = 5 \quad r_o = \frac{1}{5}\left(\sqrt{5+2\sqrt{5}}\right)\alpha_m \tag{5.68}$$

$$n = 6 \quad r_o = \frac{1}{6}\left(2+\sqrt{3}\right)\alpha_m \tag{5.69}$$

$$n = 8 \quad r_o = \frac{1}{8}\left(1+\sqrt{2}+\left(\sqrt{2-\sqrt{2}}+\sqrt{2+\sqrt{2}}\right)\right)\alpha_m \tag{5.70}$$

$$n = 10 \quad r_o = \frac{1}{10}\left(1+\sqrt{5}+\left(\sqrt{\frac{10}{4}-\frac{\sqrt{5}}{2}}+\sqrt{\frac{10}{4}+\frac{\sqrt{5}}{2}}\right)\right)\alpha_m \tag{5.71}$$

$$n = 12 \quad r_o = \frac{1}{12}\left(2+\sqrt{2}+\sqrt{3}+\left(\sqrt{2-\sqrt{3}}+\sqrt{2+\sqrt{3}}\right)\right)\alpha_m \tag{5.72}$$

There are several interesting trends seen in the equations for r_o using different values of n. The equations are functions only of α_m. Therefore, the optimum configuration for a given n depends only on the ideal separation angle according to the instantaneous weight function w_α. The shape of the parabola does not affect the results. Furthermore, with the exception of $n = 3$, the optimum radii solutions are linear functions of α_m.

The relation between r_o and n is not immediately obvious. However, upon close inspection we can determine a more general form of r_o for several values of n. For $n = 2, 4, 6$ we can express r_o as

$$r_o = \frac{1}{n}\left(\frac{n-2}{2}+\sqrt{\frac{n}{2}}\right)\alpha_m \tag{5.73}$$

A plot of the optimum radius over a range of n values is seen in Fig. 5.11. The points are the analytic solutions according to Eqs. (5.65–5.72) for $\alpha_m = 0.000375$ rad. The curve is a plot of the empirical solution in Eq. (5.73). The points for $n = 2, 4, 6$ fall exactly on the curve. This result is expected because the empirical function is derived from the equations of r_o for $n = 2, 4, 6$. The values of r_o for $n = 3, 5$ are in good agreement with the empirical

solution. However, for $n > 8$ the accuracy of the empirical function degrades. The empirical function predicts a downward trend in r_o for $n > 8$. However, the analytic solution appears to approach a limiting value.

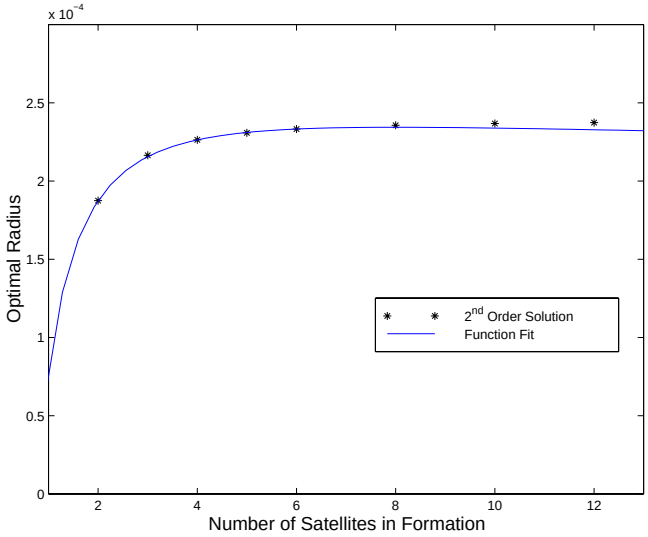

Figure 5.11: Optimum Radius for the Rotating Formation

We can determine the limit of r_o as n approaches infinity using simple geometric relations. For $n \to \infty$, $w_p(\alpha_{ij})$ is the same for all i where $i \neq j$. Therefore we only need to evaluate $w_p(\alpha_{ij})$ for an arbitrary i. Thus for $n \to \infty$ we can write

$$\tilde{W}_\infty = \lim_{n\to\infty} \frac{1}{\eta_s} \sum_{i=1}^{n-1} \sum_{j=n+1}^{n} w_p(\alpha_{ij}) = \lim_{n\to\infty} \frac{1}{n-1} \sum_{j=2}^{n} w_p(\alpha_j) \tag{5.74}$$

Figure 5.12 shows two arbitrary radius vectors, $\mathbf{r}_1$ and $\mathbf{r}_2$, defining two spacecraft positions in a circular formation. Angle r_f is the angular radius of the formation. The angle around the circle between $\mathbf{r}_1$ and $\mathbf{r}_2$ is denoted θ. Using these definitions we can write Eq. (5.74) as

$$\tilde{W}_\infty = \lim_{n\to\infty} \frac{1}{n-1} \sum_{j=2}^{n} w_p(\alpha_j) = \frac{1}{2\pi} \int_0^{2\pi} w_p(\alpha) d\theta \tag{5.75}$$

From inspection of Fig. 5.12 we can write

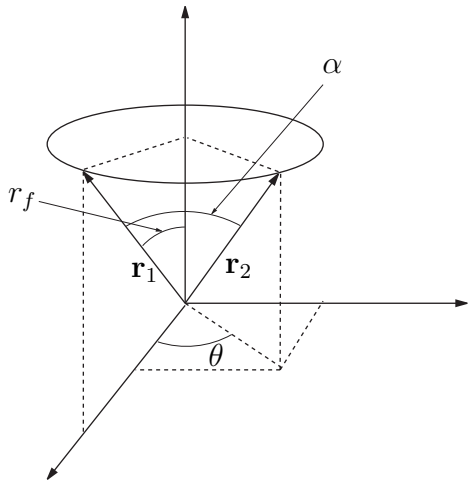

Figure 5.12: Circular Formation Geometry for $n = \infty$

$$\mathbf{r}_1 = [\sin r_f \;\; 0 \;\; \cos r_f]^T \tag{5.76}$$

$$\mathbf{r}_2 = [\sin r_f \cos\theta \;\; \sin r_f \sin\theta \;\; \cos r_f]^T \tag{5.77}$$

Recall that W_α is not dependent on the semimajor axis. Therefore we use unit vector representations of the spacecraft positions without loss of generality. Using Eq. (2.21) and the fact that $r_1 = r_2 = 1$ we can express α as

$$\alpha = \| \mathbf{r}_1 \times \mathbf{r}_2 \| \tag{5.78}$$

for small α. Substituting Eqs. (5.76–5.77) into Eq. (5.78) we obtain

$$\alpha = \sqrt{\sin^2 r_f \left(-2\cos^2 r_f \left(-1 + \cos\theta\right) + \sin^2 r_f \sin^2\theta\right)} \tag{5.79}$$

Recalling that

$$w_p = \frac{1}{\alpha_s}\left(\alpha - \alpha_u\right)\left(\alpha - \alpha_l\right) \tag{5.80}$$

and performing a substitution using Eq. (5.63) we can evaluate the integral in Eq. (5.75):

$$\begin{aligned}\tilde{W}_\infty &= \frac{1}{16\pi\alpha_s}\left(-7\pi - 16\pi\alpha_l\alpha_u + 3\pi\cos 4r_f + 8\alpha_m(k_2-k_1)\right) \\ &\quad + \frac{1}{16\pi\alpha_s}\left(4\cos 2r_f\left(\pi + 2\alpha_m(k_2-k_1)\right) + 32\alpha_m\sqrt{\sin^2 r_f}\right) \qquad (5.81)\end{aligned}$$

where k_1 and k_2 are given by

$$k_1 = \ln\left[1 - \sqrt{\sin^2 r_f}\right] \qquad (5.82)$$

$$k_2 = \ln\left[1 + \sqrt{\sin^2 r_f}\right] \qquad (5.83)$$

To solve for the optimum radius as $n \to \infty$ we need to solve

$$\frac{\partial W_\infty}{\partial r_f} = 0 \qquad (5.84)$$

However, the resulting derivative is a transcendental function in terms of α_m and r_f and cannot be explicitly solved for the optimum radius. Therefore we expand Eq. (5.81) in small r_f to second order:

$$\tilde{W}_\infty \approx \frac{1}{\alpha_s}\left(2r_f^2 - \frac{4\alpha_m r_f}{\pi} + \alpha_l\alpha_u\right) \qquad (5.85)$$

We define r_∞ as the optimum radius as $n \to \infty$. The first derivative of Eq. (5.85) with respect to r_∞ is

$$\frac{\partial\tilde{W}_\infty}{\partial r_\infty} = \frac{4}{\pi\alpha_s}\left(\pi\, r_\infty - \alpha_m\right) \qquad (5.86)$$

Setting Eq. (5.86) equal to zero and solving for r_∞ we obtain

$$r_\infty = \frac{2}{\pi}\,\alpha_m \qquad (5.87)$$

Like r_o for small n, r_∞ is only a function of α_m. Therefore the shape of the parabolic instantaneous weight function does not affect the optimum solution for large n. In Fig. 5.13

the solution of r_o for a range of n values is plotted with the asymptote r_∞. The approximation for the asymptote is in good agreement with the analytic solution for r_o for large n.

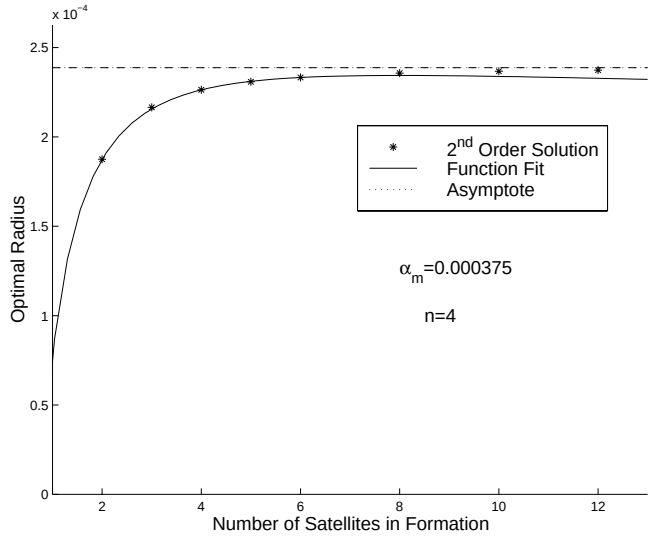

Figure 5.13: Optimum Radius with Asymptote *vs.* n

Recall that several simplifying assumptions are made to obtain an analytic solution for W_α and the limiting value as $n \to \infty$. We need to determine if the simplifications yield solutions that are in good agreement with the exact solutions. Plots of W_α for $n = 3, 4, 8, 12$ are shown in Figs. 5.14–5.15 for a range of α_m. The data points are the numerical solutions for different radii. The curves are the approximate analytic solutions for W_α. The approximate solutions are in excellent agreement with the exact solution for low α_m. For high α_m, on the order of $\alpha_m = 0.25$, accuracy of the approximate solution for W_α is poor. We expect a decrease in accuracy for high α_m because the small angle approximation was used in the development of the approximate solution. However, the optimum in performance occurs at nearly the same point according to both the exact and approximate solutions even for

$\alpha_m = 0.25$. We see in Fig. 5.16 plots of the exact *vs.* approximate optima for a range of α_m. The approximate solutions are accurate even for large α_m on the order of $\alpha_m = 0.5$. In the range of $0.5 < \alpha_m < 1$ the accuracy of the approximate solution degrades. However the approximate results are still useful in this range. We suggest that for $0.5 < \alpha_m < 1$ the approximate solutions be used as an initial guess to solve for the exact optimum using numerical techniques.

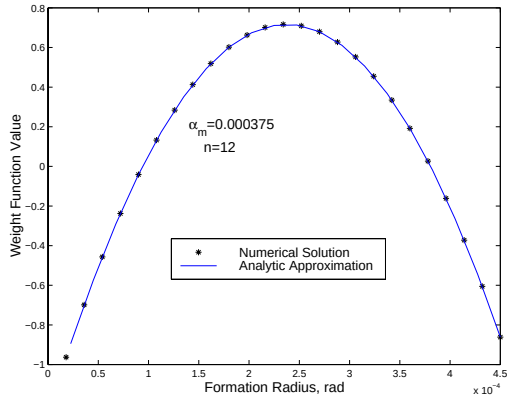

$n = 12$

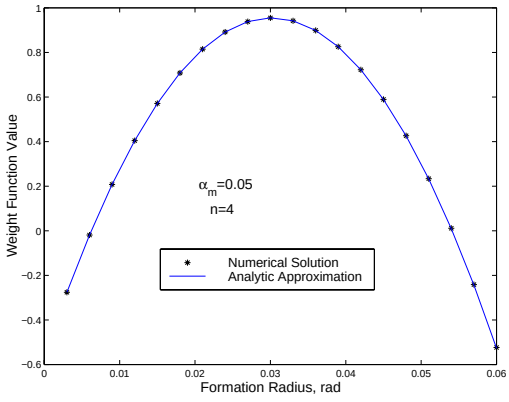

$n = 4$

Figure 5.14: Approximate and Exact Solutions for W_α

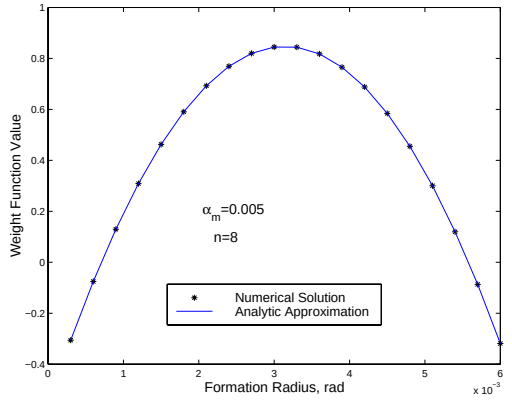

$n = 8$

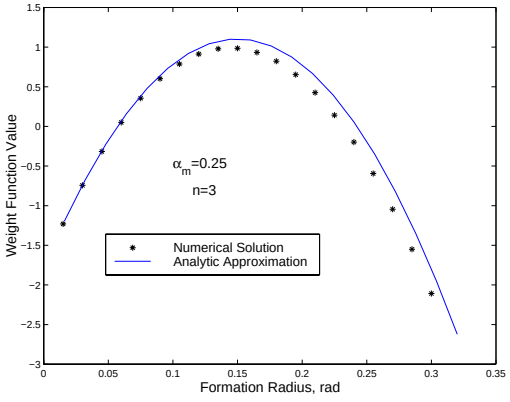

$n = 3$

Figure 5.15: Approximate and Exact Solutions for W_α

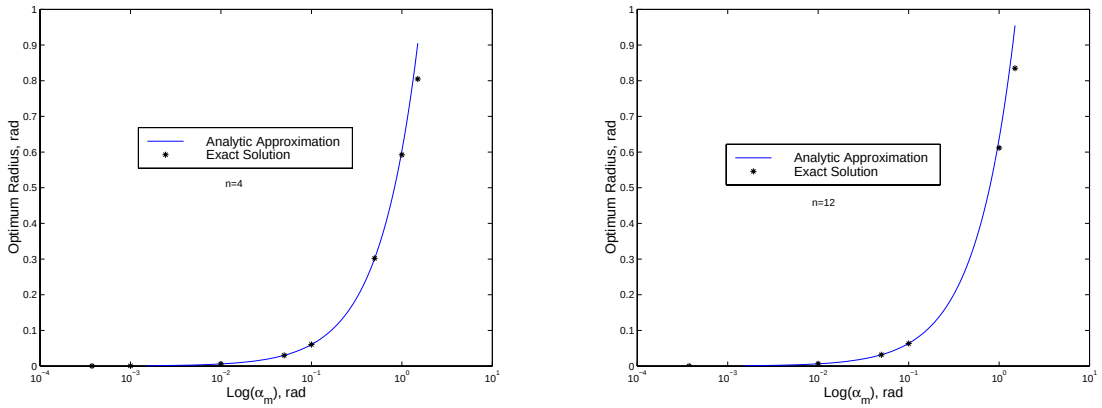

$n = 4$ $n = 12$

Figure 5.16: Approximate and Exact Optima *vs.* α_m

5.4 Summary

A formation that maintains a constant shape over an orbit has several advantages over a dynamic array such as the diamond formation. The relative positions of spacecraft in a constant shape formation are nearly constant over an orbit. Therefore the formation can be designed such that the angular separations between spacecraft are near ideal for an entire orbit. In section 5.1 we develop an algorithm to place n satellites equally spaced in time around an ellipse in the relative reference frame. In sections 5.3.1–5.3.2 we apply the orbit measures to the rotating formation using numerical techniques. An analytical expression for W_α using a parabolic instantaneous weight is developed in section 5.3.3. The exact expression is a non-trivial function of orbit eccentricity, inclination, the number of spacecraft, and the constants that define the parabolic weight. However, several simplifying assumptions allow for an analytic approximation. Using the resulting approximate equation for W_α we solve for optimal configurations for different values of n. We show that, according to W_α, the

optimal rotating formation is circular. The optimal radii for different values of n are found to be simple functions of α_m, the ideal separation angle according to the instantaneous weight function. Interestingly, the optimal configuration does not depend on the shape of the parabola. The optimal radius appears to approach a limiting value as n goes to infinity. The limit is determined to be approximately $2\alpha_m/\pi$.

Chapter 6

Approximate Results

Application of the orbit performance measures requires knowledge of the relative position of all satellites in a formation over an orbit. In Chs. 4–5 the measures are evaluated by numerically integrating the Keplerian equations of motion. However, numerical integration schemes are computationally expensive and the level of accuracy they provide may not be necessary. A closed-form analytic approximation for the relative motion of spacecraft is desirable. In this chapter we use the Clohessy-Wiltshire equations,[20] a first-order relative motion approximation, to evaluate the orbit performance measures. We investigate the differences between the exact solution obtained numerically and the approximate solution obtained from the Clohessy-Wiltshire equations.

6.1 The Clohessy-Wiltshire Equations

The Clohessy-Wiltshire equations are a first-order solution to the relative motion problem. The equations describe the motion of a spacecraft with respect to the relative reference frame, $\mathcal{F}_{rel}$, described in Ch. 5. For the derivation of the Clohessy-Wiltshire equations we define the origin of $\mathcal{F}_{rel}$ as $\mathbf{r}_t$. The spacecraft whose relative motion we are interested in, is denoted by the vector $\mathbf{r}_i$. We need to obtain an expression for $\ddot{\mathbf{r}}_{rel}$ where $\mathbf{r}_{rel}$ is given by

$$\mathbf{r}_{rel} = \mathbf{r}_i - \mathbf{r}_t \tag{6.1}$$

To do so we first find an expression for $\ddot{\mathbf{r}}_{rel}$ in the inertial system, and then apply the kinematics relation, $\ddot{\mathbf{r}}_I = \ddot{\mathbf{r}}_R + \dot{\boldsymbol{\omega}}_R \times \mathbf{r}_R + 2\,\boldsymbol{\omega}_R \times \dot{\mathbf{r}}_R + \boldsymbol{\omega}_R \times (\boldsymbol{\omega}_R \times \mathbf{r}_R)$ to find the equation of motion in the relative reference frame.

In the inertial system, the equations of motion for $\mathbf{r}_t$ and $\mathbf{r}_i$ are

$$\ddot{\mathbf{r}}_t = -\mu \frac{\mathbf{r}_t}{r_t^3} \tag{6.2}$$

$$\ddot{\mathbf{r}}_i = -\mu \frac{\mathbf{r}_i}{r_i^3} + \mathbf{F} \tag{6.3}$$

where $\mathbf{F}$ is the vector resultant of the applied forces other than gravity.

We take the second derivative of Eq. (6.1) with respect to time to obtain an expression for $\ddot{\mathbf{r}}_{rel}$:

$$\ddot{\mathbf{r}}_{rel} = \ddot{\mathbf{r}}_i - \ddot{\mathbf{r}}_t \tag{6.4}$$

Substituting Eqs. (6.2–6.3) into Eq. (6.4) yields the equation of motion of $\mathbf{r}_{rel}$ in terms of

the vectors $\mathbf{r}_t$, $\mathbf{r}_i$ and their magnitudes:

$$\ddot{\mathbf{r}}_{rel} = -\mu\frac{\mathbf{r}_i}{r_i^3} + \mathbf{F} + \mu\frac{\mathbf{r}_t}{r_t^3} \tag{6.5}$$

We need to find an expression for $\mathbf{r}_i/r_i^3$ to allow a simplification of Eq. (6.5). Rearranging Eq. (6.1) we have

$$\frac{\mathbf{r}_i}{r_i^3} = \frac{\mathbf{r}_t + \mathbf{r}_{rel}}{\parallel \mathbf{r}_t + \mathbf{r}_{rel} \parallel^3} \tag{6.6}$$

Using the law of cosines, we can write

$$\frac{1}{\parallel \mathbf{r}_t + \mathbf{r}_{rel} \parallel^3} = \frac{1}{(r_t^2 + r_{rel}^2 + 2\,\mathbf{r}_t \cdot \mathbf{r}_{rel})^{\frac{3}{2}}} \tag{6.7}$$

Equation (6.7) is not useful in this form. A Taylor series approximation to second order permits a simplification. To second order, an expansion about $\mathbf{r}_{ref} = 0$ yields

$$\frac{1}{(r_t^2 + r_{rel}^2 + 2\,\mathbf{r}_t \cdot \mathbf{r}_{rel})^{\frac{3}{2}}} = \frac{1}{a^3} - \frac{3x}{a^4} + \frac{6x^2}{a^5} - \frac{3}{2}\frac{y^2}{a^5} - \frac{3}{2}\frac{z^2}{a^5} \tag{6.8}$$

where x, y, and z are the components of $\mathbf{r}_{rel}$ in $\mathcal{F}_{rel}$. Now we return to Eq. (6.6) and substitute Eq. (6.8) to obtain the relationship,

$$\frac{\mathbf{r}_i}{r_i^3} = (\mathbf{r}_t + \mathbf{r}_{rel})\left(\frac{1}{a^3} - \frac{3x}{a^4} + \frac{6x^2}{a^5} - \frac{3}{2}\frac{y^2}{a^5} - \frac{3}{2}\frac{z^2}{a^5}\right) \tag{6.9}$$

Keeping only terms of $\mathcal{O}(2)$and grouping the components in each direction, Eq. (6.9) becomes

$$\frac{\mathbf{r}_i}{r_i^3} = \frac{\mathbf{r}_t}{r_t^3} + \frac{1}{a^3}\left(-2x + \frac{6x^2}{a} - \frac{3}{2}\frac{y^2}{a} - \frac{3}{2}\frac{z^2}{a}\right)\hat{\mathbf{i}}_{rel} + \frac{1}{a^3}\left(y - \frac{3xy}{a}\right)\hat{\mathbf{j}}_{rel} + \frac{1}{a_3}\left(z - \frac{3xz}{a}\right)\hat{\mathbf{k}}_{rel} \tag{6.10}$$

where $\hat{\mathbf{i}}_{rel}$, $\hat{\mathbf{j}}_{rel}$, and $\hat{\mathbf{k}}_{rel}$ are the unit vectors defining $\mathcal{F}_{rel}$. Finally, substituting Eq. (6.10) into Eq. (6.5) yields the desired relation for $\ddot{\mathbf{r}}_{rel}$ in the inertial frame:

$$\ddot{\mathbf{r}}_{rel} = \eta^2\left(2x - \frac{3x^2}{a} + \frac{3}{2}\frac{y^2}{a} + \frac{3}{2}\frac{z^2}{a}\right)\hat{\mathbf{i}} + \eta^2\left(-y + \frac{3xy}{a}\right)\hat{\mathbf{j}} + \eta^2\left(-z + \frac{3xz}{a}\right)\hat{\mathbf{k}} + \mathbf{F} \tag{6.11}$$

We have used Kepler's third law, $\eta^2 a^3 = \mu$, to simplify the relation.

Now we need to write $\ddot{\mathbf{r}}_{rel}$ in the rotating reference frame, knowing its inertial representation. From kinematics we know that

$$\ddot{\mathbf{r}}_I = \ddot{\mathbf{r}}_R + \dot{\boldsymbol{\omega}}_R \times \mathbf{r}_R + 2\boldsymbol{\omega}_R \times \dot{\mathbf{r}}_R + \boldsymbol{\omega}_R \times (\boldsymbol{\omega}_R \times \mathbf{r}_R) \tag{6.12}$$

Equation (6.12) gives the relation between an acceleration vector's representation in an inertial reference frame, and its representation in an arbitrary rotating reference frame. For the relative motion problem the rotating reference frame is $\mathcal{F}_{rel}$. We can solve Eq. (6.12) for the representation of $\ddot{\mathbf{r}}_{rel}$ in the rotating reference frame to give

$$\ddot{\mathbf{r}}_{rel} = \ddot{\mathbf{r}}_I - \dot{\boldsymbol{\omega}}_R \times \mathbf{r}_R - 2\boldsymbol{\omega}_R \times \dot{\mathbf{r}}_R - \boldsymbol{\omega}_R \times (\boldsymbol{\omega}_R \times \mathbf{r}_R) \tag{6.13}$$

Recalling that $\mathcal{F}_{rel}$ is defined by a circular orbit, we can determine expressions for the angular velocity $\boldsymbol{\omega}_R$ and the rate of change of angular velocity $\dot{\boldsymbol{\omega}}_R$. Specifically,

$$\boldsymbol{\omega}_R = \eta\,\hat{\mathbf{k}} \tag{6.14}$$

$$\dot{\boldsymbol{\omega}}_R = 0 \tag{6.15}$$

Substituting Eqs. (6.11), (6.14), and (6.15) into Eq. (6.13) we obtain the relationship

$$\begin{aligned} \ddot{\mathbf{r}}_{rel} \;=\; & \eta^2 \left(2x - \frac{3x^2}{a} + \frac{3}{2}\frac{y^2}{a} + \frac{3}{2}\frac{z^2}{a}\right)\hat{\mathbf{i}} + \eta^2 \left(-y + \frac{3xy}{a}\right)\hat{\mathbf{j}} + \\ & \eta^2 \left(-z + \frac{3xz}{a}\right)\hat{\mathbf{k}} + \mathbf{F} + 2\eta\dot{y}\hat{\mathbf{i}} - 2\eta\dot{x}\hat{\mathbf{j}} + \eta^2 x\hat{\mathbf{i}} + \eta^2 y\hat{\mathbf{j}} \end{aligned} \tag{6.16}$$

This is the second-order vector equation of motion of $\mathbf{r}_{rel}$ in the rotating reference frame. Extracting the components we have the three scalar equations

$$\ddot{x} - 3\eta^2 x - 2\eta\dot{y} + \frac{3\eta^2 x^2}{a} - \frac{3\eta^2 y^2}{2a} - \frac{3\eta^2 z^2}{2a} = F_x \tag{6.17}$$

$$\ddot{y} + 2\eta\dot{x} - \frac{3\eta^2 xy}{a} = F_y \tag{6.18}$$

$$\ddot{z} + \eta^2 z - \frac{3\eta^2 xz}{a} = F_z \tag{6.19}$$

The solutions to the second-order equations are not known. However, the solutions to the linear equations are known for $\mathbf{F} = 0$. Keeping only the linear terms in Eqs. (6.17–6.19) we obtain

$$\ddot{x} - 2\eta\dot{y} - 3\eta^2 x = F_x \tag{6.20}$$

$$\ddot{y} + 2\eta\dot{x} = F_y \tag{6.21}$$

$$\ddot{z} + \eta^2 z = F_z \tag{6.22}$$

The solutions to Eqs. (6.20–6.22) for $\mathbf{F} = 0$ are

$$x = \frac{\dot{x}_0}{\eta}\sin\eta t - \left(3x_0 + \frac{2\dot{y}_0}{\eta}\right)\cos\eta t + \frac{2\dot{y}_0}{\eta} + 4x_0 \tag{6.23}$$

$$y = \left(6x_0 + \frac{4\dot{y}_0}{\eta}\right)\sin\eta t + \frac{2\dot{x}_0}{\eta}\cos\eta t - (6\eta x_0 + 3\dot{y}_0)t + \left(y_0 - \frac{2\dot{x}_0}{\eta}\right) \tag{6.24}$$

$$z = z_0\cos\eta t + \frac{\dot{z}_0}{\eta}\sin\eta t \tag{6.25}$$

where x_0, y_0, and z_0 are the initial position components of r_i in $\mathcal{F}_{rel}$ and $\dot{x}_0$, $\dot{y}_0$, and $\dot{z}_0$ are the initial velocity components.

We now have an analytic approximation for the relative motion between satellites. However, we need to develop an algorithm to enable the use of the approximate solution in the evaluation of the orbit performance measures.

6.2 Propagation Using the Clohessy-Wiltshire Solution

We need to develop an algorithm to allow the propagation of a formation of satellites using Eqs. (6.23–6.25). We can write the position vector for the reference spacecraft in $\mathcal{F}_{rel}$ as

$$\mathbf{r}_{ref} = \begin{bmatrix} a & 0 & 0 \end{bmatrix}^T \tag{6.26}$$

To evaluate an orbit performance measure we require the relative position vectors between the spacecraft over an orbit. For an arbitrary spacecraft in the array, we can write the position vector, $\mathbf{r}$, in terms of $\mathbf{r}_{ref}$ and the Clohessy-Wiltshire solution as

$$\mathbf{r} = \mathbf{r}_{ref} + \mathbf{r}_{rel} = \begin{bmatrix} a+x & y & z \end{bmatrix}^T \tag{6.27}$$

To calculate x, y, and z over an orbit we need to determine the initial conditions x_0, y_0 and z_0 as well as $\dot{x}_0$, $\dot{y}_0$, and $\dot{z}_0$. This is done by determining the vectors $\mathbf{r}_{rel_0}$ and $\mathbf{v}_{rel_0}$ in the inertial frame $\mathcal{F}_I$

$$\mathbf{r}_{ref_0} = \mathbf{r}_0 - \mathbf{r}_{rel_0} \tag{6.28}$$

$$\mathbf{v}_{ref_0} = \mathbf{v}_0 - \mathbf{v}_{rel_0} \tag{6.29}$$

for a given set of initial conditions $\mathbf{r}_0$ and $\mathbf{v}_0$. These must be rotated into the frame $\mathcal{F}_{rel}$ for use in Eqs. (6.23–6.25). We construct the rotation matrix by writing the components of the unit vectors $\hat{\mathbf{i}}_{rel}$, $\hat{\mathbf{j}}_{rel}$, and $\hat{\mathbf{k}}_{rel}$ in $\mathcal{F}_I$

$$\hat{\mathbf{i}}_{rel} = \mathbf{r}_{ref_0}/a \tag{6.30}$$

$$\hat{\mathbf{j}}_{rel} = \mathbf{v}_{ref_0}/v_c \tag{6.31}$$

$$\hat{\mathbf{k}}_{rel} = \hat{\mathbf{i}}_{rel} \times \hat{\mathbf{j}}_{rel} \tag{6.32}$$

where $v_c = \sqrt{\mu/a}$. We denote the rotation matrix going from $\mathcal{F}_I$ to $\mathcal{F}_{rel}$ as $\mathbf{R}^{ri}$. The rows of $\mathbf{R}^{ri}$ are the unit vectors $\hat{\mathbf{i}}_{rel}$, $\hat{\mathbf{j}}_{rel}$, and $\hat{\mathbf{k}}_{rel}$, so we can write

$$\mathbf{R}^{ri} = \begin{bmatrix} \hat{\mathbf{i}}_{rel}^T \\ \hat{\mathbf{j}}_{rel}^T \\ \hat{\mathbf{k}}_{rel}^T \end{bmatrix} \tag{6.33}$$

The representation of $\mathbf{r}_{rel_0}$ and $\mathbf{v}_{rel_0}$ in $\mathcal{F}_{rel}$ can be obtained by a performing simple matrix multiplication by $\mathbf{R}^{ri}$.

We now have the initial conditions for the solutions to Eqs. (6.23–6.25) and can solve Eq. (6.27). This solution permits calculation of the orbit performance measures. We now investigate the effects of using the approximate solutions to evaluate W.

6.3 Approximate Calculations of the Orbit Performance Measures

Approximate and exact solutions for the performance measures are found in Figs. 6.1–6.4. In each figure the exact solution is on the left and the approximate solution is on the right. Figure 6.1 shows the application of W_α with the quartic instantaneous weight for the diagonal formation. Figures 6.2–6.3 show the application of W_α and W_d to the rotating formation with $n = 4$. Figure 6.4 shows the application of W_A to the diamond formation.

We expect to see discrepancies between the approximate solution and the exact solution

for W because the Clohessy-Wiltshire equations are only applicable for small separations. We wish to characterize the errors in the evaluation of W due to the approximate solution. The discrepancy between the two solutions increases with increasing separation because the accuracy of approximate solution is poor for large separations.

The plots of W_α using both the quartic and parabolic instantaneous weights are found in Figs. 6.1–6.2. The approximate solution is in excellent agreement with the exact solution. Even at large separations, on the order of 10 km, the plots are nearly the same. More importantly, the approximate solutions yield the same optimum points as the exact solution. For the parabolic weight $W_{max} = 0.8198$ and occurs at a longitudinal separation of 4000 m and a latitudinal separation of 4500 m. The quartic weight yields an optimum of $W_{max} = 0.7558$ and occurs for a longitudinal separation of 5500 m and a latitudinal separation of 3500 m. The quartic weight is a function of α^4 whereas the parabolic weight is a function of α^2. We therefore expect W_α with the quartic weight function to be more sensitive to propagation errors due to the linear model. This observation is confirmed by examination of Fig. 6.1 and Fig. 6.2. The difference between the exact and approximate solution is greater for the quartic weight function scenario.

The distance function, W_d, displays results similar to the results for W_α. Both techniques yield an optimum of $W_{max} = 0.9326$ at $\delta_{lon} = 3500$ m and $\delta_{lat} = 3000$ m. As expected the discrepancy between the two methods is greatest at larger separations. Careful observation reveals that W_d is more sensitive to the approximate solution than W_α. This result occurs because errors in the position solution in the radial direction do not affect the angle between

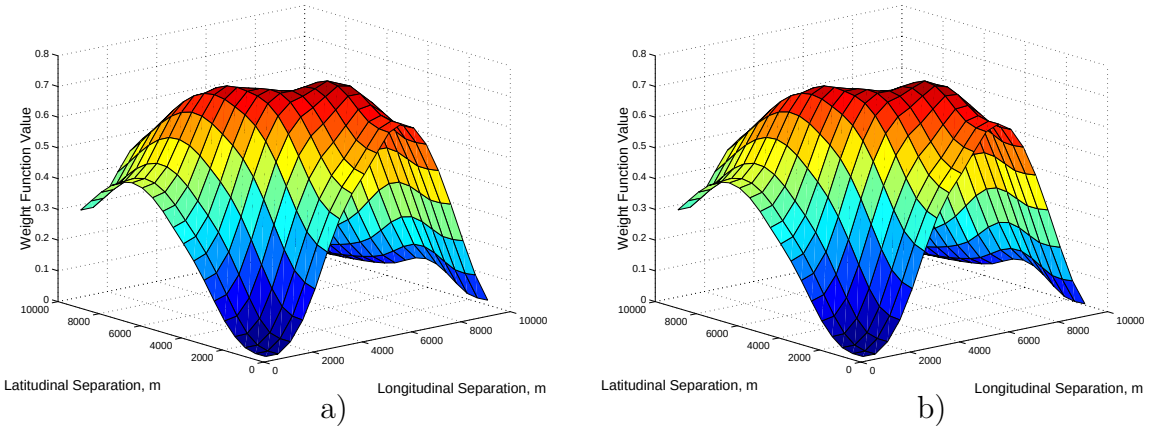

Figure 6.1: W_α Using w_q for the Diagonal Formation: a) Exact ; b) Approximate

spacecraft position vectors and therefore do not affect the solution of W_α. Errors in the radial direction do influence the instantaneous distance function and hence there is an effect on W_d.

The area function, W_A, applied to the diamond formation is plotted in Fig. 6.4. The exact solution is on the left of the figure and the approximate solution is on the right. The plots are seen to be nearly identical. According to both techniques the maximum is $W_{max} = 0.2415$ occurring for a longitudinal separation of 3000 m and a latitudinal separation of 2000 m. The area weight, similar to the angular weight, is not affected by errors in the radial direction and therefore is less sensitive to the errors introduced by the linear propagation than the distance measure.

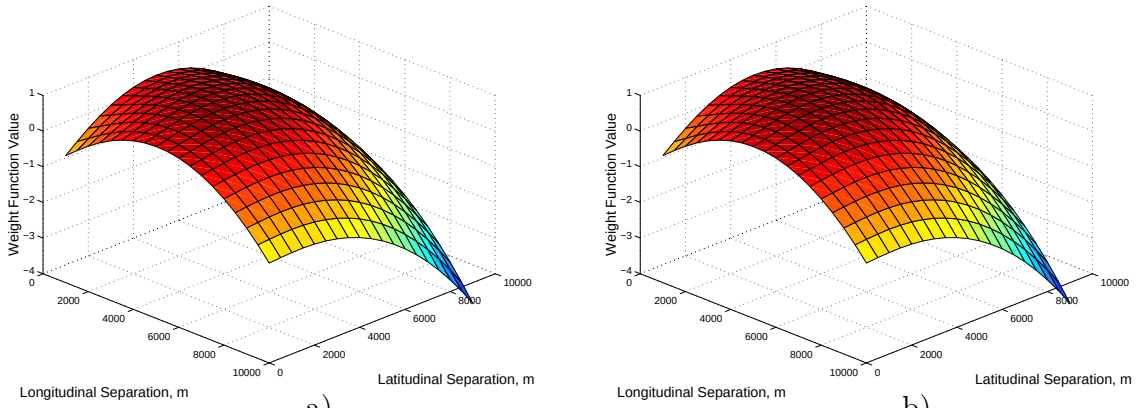

Figure 6.2: W_α Using w_p for the Rotating Formation: a) Exact ; b) Approximate

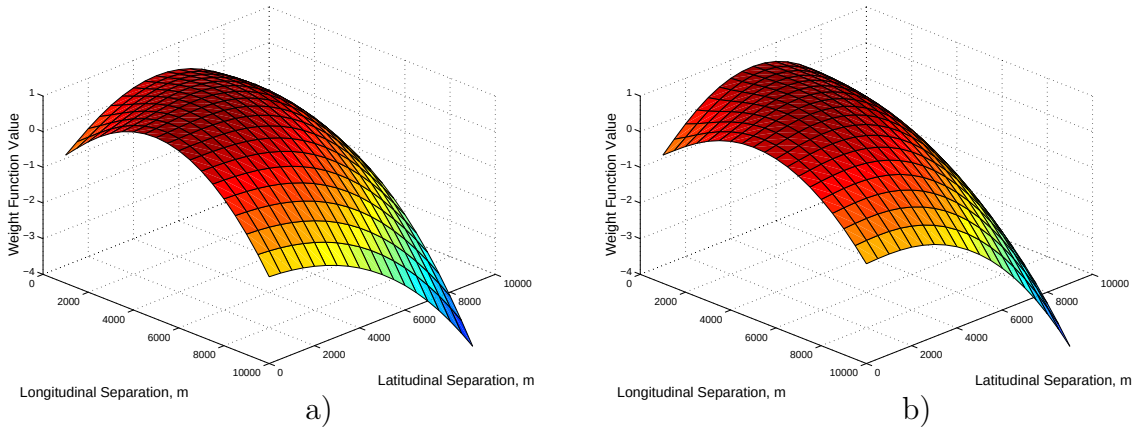

Figure 6.3: W_d Applied to the Rotating Formation: a) Exact ; b) Approximate

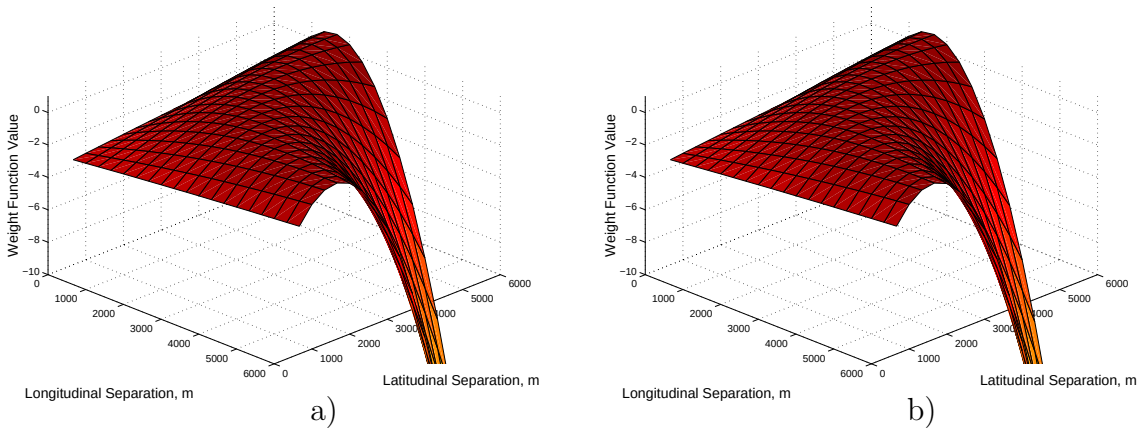

Figure 6.4: W_A Applied to the Diagonal Formation: a) Exact ; b) Approximate

6.4 Summary

Application of the orbit performance measures requires the relative position of all satellites in the formation over an orbit period. The relative positions can be calculated by numerically integrating the equations of motion. However, numerical integration is costly and the level of accuracy compared to approximate solutions is not required to evaluate the orbit performance measures. We see that the same optimum solution to the orbit performance measures is obtainable using the Clohessy-Wiltshire approximation. Interestingly, W_d is more sensitive to approximate techniques than W_α and W_A. This result occurs because errors in the radial direction do not affect the angular separation or the instantaneous separation area.

Chapter 7

Conclusions

In this thesis we develop two types of performance measures for formation flying missions: instantaneous measures that allow an investigation of a formation configuration at a particular instant, and orbit measures that allow an investigation into the performance of a formation over an orbit period. The overlap area (IOA) is an instantaneous measure defined as the area on the sphere that can be viewed simultaneously by all spacecraft in formation. The calculation of the overlap area requires extensive application of spherical trigonometry relations. The overlap area provides a measure of the "closeness" between spacecraft in formation. We define a second instantaneous measure we call the separation area (ISA). The separation area is defined as the area enclosed by connecting the outer-most subsatellite points with great circles. Calculation of the separation area is simple because it is bordered by great circles. Contrary to the IOA, the ISA provides a measure of the "separation" between spacecraft in formation.

In Ch. 3 we develop orbit performance measures based on the integration of an instantaneous position metric over an orbit period. The instantaneous metrics are functions of the desired spatial or angular separations between spacecraft in formation. We also develop an orbit measure based on a weighted average of the desired separation area. For the angular separation metric we consider two forms for the instantaneous position metric: a quartic form, and a quadratic form. For the distance and separation area measures we assume a parabolic form for the instantaneous metric.

In Ch. 4 we develop a formation we call the diamond formation. The formation is composed of four spacecraft in circular orbits with common semimajor axes. Two of the spacecraft are in coplanar orbits. The other two spacecraft are in orbits equally inclined with respect to the coplanar orbits. Optimal configurations of the diamond formation are determined for each performance measure. We also investigate the effects of changing orbit parameters such as the semimajor axis and eccentricity on the performance measures. The measures are shown to be independent of the semimajor axis. However, the effects of eccentricity are complex and dependent on the formation configuration. We also consider a more general diamond formation model and an optimal configuration is determined using Newton's Method.

A formation that maintains a constant shape over an orbit has several advantages over a dynamic array such as the diamond formation. The relative positions of spacecraft in a constant shape formation are nearly constant over an orbit. Therefore the formation can be designed such that the angular separations between spacecraft are near ideal for an entire

orbit. We develop an algorithm to place n satellites equally spaced in time around an ellipse in the relative reference frame. We apply the orbit measures to the rotating formation using numerical techniques. An analytical expression for W_α using a parabolic instantaneous weight is also developed. The exact expression is a non-trivial function of eccentricity, inclination, the number of spacecraft, and the constants that define the parabolic weight. However, several simplifying assumptions allow for an analytic approximation. Using the resulting approximate equation for W_α we solve for optimal configurations in terms of the number of spacecraft. We show that according to W_α, the optimal rotating formation is circular. The optimal radii for different values of n are found to be simple functions of α_m, the ideal separation angle according to the instantaneous weight function. Interestingly, the optimal configuration does not depend on the shape of the parabola. The optimal radius appears to approach a limiting value as n goes to infinity. The limit is determined to be approximately $2/\pi$. To determine the validity of the approximate solutions they are compared with the exact numerical solutions for a range of α_m. The analytic solutions for $e < 0.5$ are in excellent agreement with the numerical solutions. For $e > 0.05$ the analytic solutions are less accurate however, they are still useful. We suggest that for $\alpha_m > 0.5$ the approximate solutions be used as an initial guess to solve for the exact optimum using numerical techniques.

Application of the orbit performance measures requires the relative position of all satellites in the formation over an orbit period. In general the orbit measures do not permit an analytic solution. The relative positions can be calculated by numerically integrating

the equations of motion. However, numerical integration is costly and the level of accuracy compared to approximate solutions is not necessary to obtain accurate solutions for the orbit performance measures. We show that the same optimum solutions for the three orbit performance measures are obtainable using the Clohessy-Wiltshire approximations.

There are several areas of this research we recommend for further investigation. An extension of the orbit performance measures to include the physical requirements of remote sensing geometry requirements is desirable. Specifically, we wish to include the perspective angle α_p, discussed in Ch. 3, explicitly in the orbit measures. The solution to the performance problem can then be investigated directly in terms of the desirable range of α_p. We also recommend developing an analytic solution to the distance-based orbit measure using the same approach as that used for the angular separation measure. Also, an investigation of perturbations, especially the effects of J_2, on performance is an important question that remains unanswered.

Appendix A

Nomenclature

A_{inner}	inner overlap area, m^2
A_l	lower limit on separation area, m^2
A_{lune}	area of a lune, m^2
A_m	ideal separation area, m^2
A_n	scaling factor, m^2
A_o	overlap area, m^2
A_{outer}	outer overlap area, m^2
A_{refo}	reference overlap area, m^2
A_{refs}	reference separation area, m^2
A_s	separation area, m^2
A_u	upper limit on separation area, m^2

a	semimajor axis, m
c_1, c_2, c_3	constants defining parabolic weight
d	spatial separation between two spacecraft, m
d_l	lower limit on spatial separation, m
d_{lat}	formation latitudinal separation, m
d_{lon}	formation longitudinal separation, m
d_m	ideal spatial separation, m
d_u	upper limit on spatial separation, m
d_s	scaling factor, m
e	orbit eccentricity
e_{opt}	eccentricity to provide optimum performance
$\mathcal{F}_I$	inertial reference frame
$\mathcal{F}_{rel}$	relative reference frame
$\mathcal{F}_R$	rotating reference frame
$\mathcal{F}_p$	perifocal reference frame
$\mathcal{F}_s$	intermediate reference frame
i	orbit inclination, rad
i_{opt}	inclination to provide optimum performance, rad
ℓ	true longitude at epoch, rad
n	number of spacecraft in formation
n_p	number of points defining overlap region

R_e	Earth radius, m
R_r	range vector from spacecraft to target, m
r_∞	optimum radius as $n \to \infty$, rad
r_o	optimum radius for rotating formation, rad
T	orbital period, s
t_i	propagation time for i^{th} spacecraft, s
t_s	equal time separation for n spacecraft, s
u	argument of latitude at epoch, rad
W	orbit performance measure
W_∞	W_α as $n \to \infty$
W_a	approximate expression for W_α
w	instantaneous position metric
α	angular separation between two spacecraft, rad
α_{ij}	angle between the i^{th} and j^{th} satellites, rad
α_l	lower limit on angular separation, rad
α_m	ideal angular separation, rad
α_p	perspective angle, rad
α_s	scaling factor, rad
α_u	upper limit on angular separation, rad
β	angle between sub-satellite points, rad
δ	minimum elevation angle, rad

δ_{lon}	formation longitudinal separation, rad
δ_{lat}	formation latitudinal separation,rad
η	orbit mean motion, rad/s
η_s	number of distinct angles in a formation
θ	rotation angle of inner overlap area, rad
λ	Earth central angle, rad
μ	gravitational parameter, m^3/s^2
ν	true anomaly, rad
ρ,ϵ	angular radii of horizon circles, rad
Ω	longitude of ascending node, rad
ω	argument of periapsis, rad

Bibliography

[1] Adams, J., Robertson, A., Zimmerman, K., and How, J., "Technologies for Spacecraft Formation Flying," In *Proceedings of the Institute of Navigation GPS*, 1996, pp. 1321–1330.

[2] Decou, A. B., "Orbital Station-Keeping for Multiple Spacecraft Interferometry," *Journal of the Astronautical Sciences*, Vol. 39, No. 3, 1991, pp. 283–297.

[3] Folta, D. C., Bordi, F., and Scolese, C., "Considerations on Formation Flying Separations for Earth Observing Satellite Missions," *Advances in Astronautical Sciences*, Vol. 79, No. 2, 1992, pp. 803–822.

[4] Folta, D. C., Bordi, F., and Scolese, C., "Field of View Location for Formation Flying Polar Orbiting Missions," *Advances in Astronautical Sciences*, Vol. 75, No. 2, 1991, pp. 949–965.

[5] Folta, D. C., Newman, L. K., and Gardner, T., "Foundations of Formation Flying for Mission to Planet Earth and New Millennium," In *Astrodynamics Conference Proceedings*, 1996, pp. 656–666.

[6] Gramling, C. J., Lee, T., Niklewski, D. J., and Long, A. C., "Relative Navigation for Autonomous Formation Flying Spacecraft," *Advances in Astronautical Sciences*, Vol. 97, No. 1, 1998, pp. 405–431.

[7] Hartman, K. R., Gramling, C. J., Lee, T., Kelbel, D. A., and Long, A. C., "Relative Navigation for Spacecraft Formation Flying," *Advances in Astronautical Sciences*, Vol. 100, No. 2, 1998, pp. 685–699.

[8] Guinn, J. R. and Boain, R. J., "Spacecraft Autonomous Navigation for Formation Flying Earth Orbiters Using GPS," In *Astrodynamics Conference Proceedings*, 1996, pp. 722–732.

[9] How, J. P., Twiggs, R., Weidow, D., Hartman, K., and Bauer, F., "Orion: A Low-Cost Demonstration of Formation Flying in Space Using GPS," In *Astrodynamics Conference Proceedings*, 1998, pp. 276–286.

[10] Barden, B. and K.C.Howell,, "Formation Flying in the Vicinity of Libration Point Orbits," *Advances in the Astronautical Sciences*, Vol. 99, No. 2, 1998, pp. 969–988.

[11] Guinn, J. R., "Precise Relative Motions of Formation Flying Vehicles," In *Astrodynamics Conference Proceedings*, 1998, pp. 34–39.

[12] Folta, D. C. and Quinn, D. A., "Enhanced Formation Flying For the Earth Observing-1(EO-1) New Millenium Mission," In *NASA Conference Publication*, volume 3345, 1997, pp. 405–427.

[13] Folta, D. C. and Quinn, D. A., "An Algorithm for Enhanced Formation Flying of Satellites in Low Earth Orbit," In *AIP Conference Proceedings*, volume 420, 1998, pp. 119–126.

[14] Wickert, D. P., Shaw, G. B., and Hastings, D., "Impact of a Distributed Architechture for Space-Based Radar," *Journal of Spacecraft and Rockets*, Vol. 35, No. 5, 1998, pp. 703–713.

[15] Chichka, D. F., "Dynamics of Clustered Satellites via Orbital Elements," In *AAS/AIAA Astrodynamics Conference Proceedings*, 1999, pp. 969–988.

[16] Bate, R. R., Mueller, D. D., and White, J. E., *Fundamentals of Astrodynamics*, Dover, New York, 1971.

[17] Larson, W. J. and Wertz, J. R., *Space Mission Analysis and Design*, Microcosm Inc., Torrance, 1992.

[18] Smart, W. M., *Textbook on Spherical Astronomy*, University Press, Cambridge, 1962.

[19] Stoer, J. and Bulirsch, R., *Introduction to Numerical Analysis*, Springer, New York, 1993.

[20] Vallado, D. A., *Fundamentals of Astrodynamics and Applications*, McGraw-Hill, New York, 1997.

Vita

Steven Patrick Hughes was born on July 31, 1973 to parents David George and Jane Elizabeth Hughes. He is the oldest of three children including a sister Amy Elizabeth and a brother Kevin Michael. He grew up in Midlothian Virginia, a suburb of Richmond. He graduated from Clover Hill High School in 1991. From 1991 through 1994 he studied physics at Virginia Commonwealth University. In 1994 he transferred to Virginia Polytechnic Institute and State University (VT) and changed majors to Aerospace Engineering. He graduated with a Bachelor of Science in Aerospace Engineering in 1997. From 1997-1999 he continued his study of Aerospace Engineering at VT and obtained a Master of Science in Aerospace Engineering. For the summers of 1998 and 1999 he was a visiting student at NASA's Goddard Space Flight Center. His extracurricular activities include music, both listening and performing, the outdoors, including, jogging, fishing, hiking, and canoeing, as well as movies, travel and many other things.